

A high order special relativistic hydrodynamic and magnetohydrodynamic code with space-time adaptive mesh refinement

Olindo Zanotti^{a,*}, Michael Dumbser^a

^a*Laboratory of Applied Mathematics, Department of Civil, Environmental and Mechanical Engineering, University of Trento, Via Mesiano 77, I-38123 Trento, Italy*

Abstract

We present a high order one-step ADER-WENO finite volume scheme with space-time adaptive mesh refinement (AMR) for the solution of the special relativistic hydrodynamic and magnetohydrodynamic equations. By adopting a local discontinuous Galerkin predictor method, a high order one-step time discretization is obtained, with no need for Runge–Kutta sub-steps. This turns out to be particularly advantageous in combination with space-time adaptive mesh refinement, which has been implemented following a “cell-by-cell” approach. As in existing second order AMR methods, also the present higher order AMR algorithm features time-accurate local time stepping (LTS), where grids on different spatial refinement levels are allowed to use different time steps.

We also compare two different Riemann solvers for the computation of the numerical fluxes at the cell interfaces. The new scheme has been validated over a sample of numerical test problems in one, two and three spatial dimensions, exploring its ability in resolving the propagation of relativistic hydrodynamical and magnetohydrodynamical waves in different physical regimes. The astrophysical relevance of the new code for the study of the Richtmyer–Meshkov instability is briefly discussed in view of future applications.

Keywords: magnetohydrodynamics, special relativity, high order ADER-WENO finite volume scheme, space-time Adaptive Mesh Refinement (AMR), time-accurate local time stepping (LTS)

1. Introduction

The numerical modeling of complex astrophysical flows that involve relativistic processes requires the development of more and more sophisticated codes. Relevant examples of relativistic phenomena whose understanding can greatly benefit from hydrodynamic and magnetohydrodynamic numerical simulations include extragalactic jets, gamma-ray-bursts, accretion onto compact objects, binary mergers of neutron stars (or black holes), relativistic heavy-ion collisions and so on.

*Corresponding author

Email addresses: olindo.zanotti@unitn.it (Olindo Zanotti), michael.dumbser@unitn.it (Michael Dumbser)

Preprint submitted to Computer Physics Communications

October 4, 2018

Until few years ago, most of the applications in numerical relativistic hydrodynamic (RHD) and magnetohydrodynamic (RMHD) used second-order accurate, typically TVD, numerical codes. The scientific progress that has been made possible by these implementations is rather significant and not always appreciated enough, see the living reviews by Martí and Müller (2003) and by Font (2008) plus references therein. However, the necessity of improving the accuracy of the computations, especially in the presence of complex phenomena such as instabilities or turbulence, combined with computational resources which are inevitably always limited, has motivated a strong research effort along two different directions. The first direction is represented by the development of high order schemes (better than second order in space and time), while the second direction consists in the implementation of efficient adaptive mesh refinement (AMR) algorithms. Taken separately, high order numerical schemes and AMR techniques have a long history, which is embarrassing to summarize in few words. The first high order special relativistic numerical scheme is due to Dolezal (1995), who, in the context of ultra-relativistic nuclear collision experiments, implemented a conservative finite difference scheme using ENO reconstruction in space and Runge–Kutta time integration, but without Riemann solvers. The first transposition of this approach to the astrophysical context is due to Del Zanna and Bucciantini (2002), who, in addition, used local Riemann problems to guarantee the upwind character of the scheme. Since then, several high order schemes have been proposed and applied to a variety of different astrophysical problems, with and without magnetic fields, both in the special and in the general relativistic regime [see Del Zanna et al. (2003), Del Zanna et al. (2007), Tchekhovskoy et al. (2007), Bucciantini and Del Zanna (2011), Radice and Rezzolla (2011), Radice and Rezzolla (2012)]. Though different under many respects, a common feature of all these approaches is the use of a multi-step Runge–Kutta time integrator. A few years ago, Dumbser et al. (2008b) proposed an alternative idea for obtaining a high order integration in time, that avoids Runge–Kutta schemes altogether and originates from the ADER philosophy of Toro and Titarev (2002). According to this idea, which is followed also in this work, an arbitrary high order numerical scheme with just one step for the time update can be obtained, provided a high order time evolution is performed locally (namely within each cell), for the reconstructed polynomials. The first implementation of such ADER schemes in the context of ideal relativistic magnetohydrodynamics can be found in Dumbser et al. (2008a) and has later been successfully extended also to the non-ideal relativistic MHD equations in Dumbser and Zanotti (2009).

The implementation of AMR techniques has also a rich tradition in relativistic hydrodynamics and magnetohydrodynamics.¹ The first occurrence is documented in Winkler et al. (1984) followed by Dönmez (2004), Evans et al. (2005), van der Holst et al. (2008), Tao et al. (2008), Etienne et al. (2010), De Colle et al. (2012), Liebling et al. (2010), Lehner et al. (2012), East et al. (2012).

The combination of high order relativistic codes with AMR has a much more recent history. Relevant examples are given by the works of Mignone et al. (2012), who combined the AMR library CHOMBO, which originated from the original work of Berger and Olinger (1984), Berger (1986) and Berger and Colella (1989), with the versatile PLUTO code, using a Corner-Transport-Upwind scheme together with a third-order WENO reconstruction in space; Anderson et al. (2006), who solved the equations of general relativistic magnetohydrodynamics using a conservative finite difference scheme (with reconstruction of primitive variables plus Riemann solvers); Zhang and MacFadyen (2006), who implemented both a conservative finite difference scheme

¹We are not mentioning here the whole family of AMR implementations in vacuum space-times, namely without matter, which were initiated by Choptuik (1989).

(with reconstruction of fluxes and no need for Riemann solvers) and a finite volume method, within the block-structured AMR package PARAMESH of MacNeice et al. (2000).

Contrary to the above mentioned approaches, all of them sharing a TVD Runge–Kutta for the time integration, in this paper we present an ADER-WENO finite volume scheme for solving the special relativistic magnetohydrodynamics equations, with adaptive mesh refinement. In Dumbser et al. (2013) we have proposed the first ADER-AMR finite volume numerical scheme for the Newtonian Euler equations and here we propose the relativistic extension of our new approach. The use of a one-step scheme in time allows the implementation of time-accurate local time stepping (LTS) in a very natural and straight forward manner and has already been successfully applied in the context of high order Discontinuous Galerkin schemes with LTS (see Dumbser et al. (2007); Taube et al. (2009); Lörcher et al. (2007); Gassner et al. (2008)).

The outline of this paper is the following. In Sect. 2 we briefly recall the conservative formulation of special relativistic hydrodynamics. Sect. 3 is devoted to the description of the numerical method, while Sect. 4 contains the results of the new scheme. Finally, Sect. 5 concludes our work, with a discussion about future astrophysical applications. In the following we will assume a signature $\{-, +, +, +\}$ for the space-time metric and we will use Greek letters μ, ν, λ, \dots (running from 0 to 3) for four-dimensional space-time tensor components, while Latin letters i, j, k, \dots (running from 1 to 3) will be employed for three-dimensional spatial tensor components. Moreover, we set the speed of light $c = 1$ and we adopt the Lorentz-Heaviside notation for the electromagnetic quantities, such that all $\sqrt{4\pi}$ factors disappears.

2. Special relativistic magnetohydrodynamics

In the following we consider a perfect magneto-fluid, under the assumption of infinite conductivity (ideal RMHD), in a Minkowski space-time with Cartesian coordinates, for which the metric is given by

$$ds^2 = g_{\mu\nu} dx^\mu dx^\nu = -dt^2 + dx^2 + dy^2 + dz^2. \quad (1)$$

The fluid is described by an energy momentum tensor $T^{\alpha\beta}$

$$T^{\alpha\beta} = (\rho h + b^2) u^\alpha u^\beta + (p + b^2/2) g^{\alpha\beta} - b^\alpha b^\beta, \quad (2)$$

where u^α is the four-velocity of the fluid, b^α is the four-vector of the magnetic field, $b^2 = b_\alpha b^\alpha$, while ρ , $h = 1 + \epsilon + p/\rho$, ϵ and p are the rest-mass density, the specific enthalpy, the specific internal energy, and the thermal pressure, respectively. All these quantities are measured in the co-moving frame of the fluid. We assume the pressure is related to ρ and ϵ through the ideal-gas equation of state (EOS), i.e.

$$p = \rho\epsilon(\gamma - 1), \quad (3)$$

where γ is the (constant) adiabatic index of the gas. The equations of special relativistic magnetohydrodynamics, can be written in covariant form simply as

$$\nabla_\alpha(\rho u^\alpha) = 0, \quad (4)$$

$$\nabla_\alpha T^{\alpha\beta} = 0, \quad (5)$$

$$\nabla_\alpha F^{*\alpha\beta} = 0, \quad (6)$$

where $F^{*\alpha\beta}$ is the dual of the electromagnetic tensor (Anile, 1990). However, for numerical purposes it is convenient to recast them in conservative form as (Martí et al., 1991; Komissarov,

1999; Balsara, 2001)

$$\partial_t \mathbf{u} + \partial_i \mathbf{f}^i = 0, \quad (7)$$

where the conserved variables and the corresponding fluxes in the i direction are given by

$$\mathbf{u} = \begin{bmatrix} D \\ S_j \\ U \\ B^j \end{bmatrix}, \quad \mathbf{f}^i = \begin{bmatrix} v^i D \\ W_j^i \\ S^i \\ \epsilon^{ijk} E^k \end{bmatrix}. \quad (8)$$

The conserved variables (D, S_j, U, B_j) are related to the rest-mass density ρ , to the thermal pressure p , to the fluid velocity v_i and to the magnetic field B_i by²

$$D = \rho W, \quad (9)$$

$$S_i = \rho h W^2 v_i + \epsilon_{ijk} E_j B_k, \quad (10)$$

$$U = \rho h W^2 - p + \frac{1}{2}(E^2 + B^2), \quad (11)$$

where ϵ_{ijk} is the Levi–Civita tensor and δ_{ij} is the Kronecker symbol. We have used $W = (1 - v^2)^{-1/2}$ to denote the Lorentz factor of the fluid with respect to the Eulerian observer at rest in the Cartesian coordinate system, while E_i are the components of the electric field, which, in ideal magnetohydrodynamics, is simply given by $\vec{E} = -\vec{v} \times \vec{B}$. The tensor

$$W_{ij} \equiv \rho h W^2 v_i v_j - E_i E_j - B_i B_j + \left[p + \frac{1}{2}(E^2 + B^2) \right] \delta_{ij} \quad (12)$$

is the fully spatial projection of the energy-momentum tensor of the fluid [see also Del Zanna et al. (2007)]. In order to preserve the divergence-free property of the magnetic field, we augment the system (7) with an additional equation for a scalar field Φ , whose role is to propagate away the deviations from $\vec{\nabla} \cdot \vec{B} = 0$. In practice, we need to solve

$$\partial_t \Phi + \partial_i B^i = -\kappa \Phi, \quad (13)$$

while the fluxes for the evolution of the magnetic field are also modified, namely $\mathbf{f}^i(B^j) \rightarrow \epsilon^{jik} E^k + \Phi \delta^{ij}$. This approach has been introduced by Dedner et al. (2002) for the classical MHD equations, and it has been later extended to the relativistic regime by Palenzuela et al. (2009). We emphasize that the damping coefficient κ in Eq. (13) drives the solution towards $\vec{\nabla} \cdot \vec{B} = 0$ over a timescale $1/\kappa$. In our simulations with a non-zero magnetic field we have used $\kappa \in [1; 10]$ (see also Dionysopoulou et al. (2013)). As a hyperbolic system in conservative form, the equations (7) admit a well defined Jacobian matrix with a corresponding set of eigenvectors and eigenvalues. All these properties have been investigated deeply over the years. We address the interested reader to Aloy et al. (1999); Martí and Müller (2003); Rezzolla and Zanotti (2013) and to Balsara and Spicer (1999); Komissarov (1999); Del Zanna et al. (2007); Antón et al. (2010) for the mathematical aspects of the RHD and of the RMHD equations, respectively. We just comment here on the method adopted to invert the system (9)–(11), which is needed to recover the

²We note that, since the spacetime is flat and we are using Cartesian coordinates, the covariant and the contravariant components of spatial vectors can be used interchangeably, namely $A_i = A^i$, for the generic vector \vec{A} .

primitive variables (p, ρ, v_i, B_i) from the conserved variables (D, S_i, U, B_i) . As well known, in the relativistic framework such a conversion is not analytic, and a numerical root-finding approach is therefore needed. In our numerical code we have at disposal two alternative strategies. The first one is due to Del Zanna et al. (2007), and it can be used both in the case of purely RHD systems and of RMHD systems. It is based on the property that, after introducing the variables $x = v^2$, $y = \rho h W^2$, the whole problem can be reduced to the solution of the system $F_1 = 0$ and $F_2 = 0$, where

$$F_1(x, y) = x(y + B^2)^2 - y^{-2}(S_i B^i)^2(2y + B^2) - S^2, \quad (14)$$

$$F_2(x, y) = y - p + \frac{1}{2}(1 + x)B^2 - \frac{1}{2}y^{-2}(S_i B^i)^2 - U, \quad (15)$$

where $S^2 = S^i S_i$, $B^2 = B^i B_i$. Moreover, since the pressure of the ideal gas EOS (3) can be written as

$$p = \frac{\gamma - 1}{\gamma} [y(1 - x) - D \sqrt{1 - x}], \quad (16)$$

the second equation of the system above, namely Eq. (15), further reduces to an equation in the single unknown y , which can be solved with any root-finding algorithm. We emphasize that this strategy is our only choice when magnetic fields are present. The second strategy that we have implemented can instead be used only for RHD systems and it is very similar to that of Baiotti (2004) [see also Appendix D of Rezzolla and Zanotti (2013)]. It requires the numerical solution of the following equation

$$p - \bar{p}[\rho(\mathbf{u}, p), \epsilon(\mathbf{u}, p)] = 0, \quad (17)$$

where p is the unknown pressure and \bar{p} is the pressure as obtained through the equation of state (3) written in terms of the conserved variables \mathbf{u} and of p itself. In both the strategies just described, the standard Newton–Raphson method has been adopted, combined to a bisection step for those cases when the Newton–Raphson fails. We emphasize that, for flows with large Lorentz factors, i.e. $W \geq 10$, the second strategy behaves better than the first one, which instead manifests a higher failure rate. In Sect. 3.1 we discuss the strategy undertaken when such failures occur.

3. Numerical method

As written like in Eq. (7), the equations of special relativistic hydrodynamics can be solved through a modern version of the ADER approach, namely by combining a high order WENO reconstruction in space with a local space-time Galerkin predictor strategy for the time update. In the following we provide a concise explanation of the overall procedure, addressing to the relevant literature for an extended discussion, and especially to Dumbser et al. (2008b), Dumbser and Zanotti (2009) and Dumbser et al. (2013).

3.1. The Finite volume approach

According to the standard finite volume approach, a one-step discretization of the system of hyperbolic conservation laws (7) is obtained by integration of the PDE over a space-time control volume $C_{ijkn} = [x_{i-\frac{1}{2}}; x_{i+\frac{1}{2}}] \times [y_{j-\frac{1}{2}}; y_{j+\frac{1}{2}}] \times [z_{k-\frac{1}{2}}; z_{k+\frac{1}{2}}] \times [t^n; t^{n+1}]$ as³

$$\bar{\mathbf{u}}_{ijk}^{n+1} = \bar{\mathbf{u}}_{ijk}^n - \frac{\Delta t}{\Delta x_i} (\mathbf{f}_{i+\frac{1}{2},jk} - \mathbf{f}_{i-\frac{1}{2},jk}) - \frac{\Delta t}{\Delta y_j} (\mathbf{g}_{i,j+\frac{1}{2},k} - \mathbf{g}_{i,j-\frac{1}{2},k}) - \frac{\Delta t}{\Delta z_k} (\mathbf{h}_{i,j,k+\frac{1}{2}} - \mathbf{h}_{i,j,k-\frac{1}{2}}) \quad (18)$$

³To keep the notation simpler, in the following we avoid the Einstein summation convention for the flux components, by writing explicitly $\mathbf{f} = \mathbf{f}^x, \mathbf{g} = \mathbf{f}^y, \mathbf{h} = \mathbf{f}^z$.

where

$$\bar{\mathbf{u}}_{ijk}^n = \frac{1}{\Delta x_i} \frac{1}{\Delta y_j} \frac{1}{\Delta z_k} \int_{x_{i-\frac{1}{2}}}^{x_{i+\frac{1}{2}}} \int_{y_{j-\frac{1}{2}}}^{y_{j+\frac{1}{2}}} \int_{z_{k-\frac{1}{2}}}^{z_{k+\frac{1}{2}}} \mathbf{u}(x, y, z, t^n) dz dy dx \quad (19)$$

is the spatial average of the solution in the element $I_{ijk} = [x_{i-\frac{1}{2}}; x_{i+\frac{1}{2}}] \times [y_{j-\frac{1}{2}}; y_{j+\frac{1}{2}}] \times [z_{k-\frac{1}{2}}; z_{k+\frac{1}{2}}]$ at time t^n , while

$$\mathbf{f}_{i+\frac{1}{2},jk} = \frac{1}{\Delta t} \frac{1}{\Delta y_j} \frac{1}{\Delta z_k} \int_{t^n}^{t^{n+1}} \int_{y_{j-\frac{1}{2}}}^{y_{j+\frac{1}{2}}} \int_{z_{k-\frac{1}{2}}}^{z_{k+\frac{1}{2}}} \tilde{\mathbf{f}}_{\text{RP}}(x_{i+\frac{1}{2}}, y, z, t) dz dy dt, \quad (20)$$

$$\mathbf{g}_{i,j+\frac{1}{2},k} = \frac{1}{\Delta t} \frac{1}{\Delta x_i} \frac{1}{\Delta z_k} \int_{t^n}^{t^{n+1}} \int_{x_{i-\frac{1}{2}}}^{x_{i+\frac{1}{2}}} \int_{z_{k-\frac{1}{2}}}^{z_{k+\frac{1}{2}}} \tilde{\mathbf{g}}_{\text{RP}}(x, y_{j+\frac{1}{2}}, z, t) dz dx dt, \quad (21)$$

$$\mathbf{h}_{ij,k+\frac{1}{2}} = \frac{1}{\Delta t} \frac{1}{\Delta x_i} \frac{1}{\Delta y_j} \int_{t^n}^{t^{n+1}} \int_{x_{i-\frac{1}{2}}}^{x_{i+\frac{1}{2}}} \int_{y_{j-\frac{1}{2}}}^{y_{j+\frac{1}{2}}} \tilde{\mathbf{h}}_{\text{RP}}(x, y, z_{k+\frac{1}{2}}, t) dy dx dt \quad (22)$$

are the space–time averaged numerical fluxes, with $\tilde{\mathbf{f}}_{\text{RP}}(x_{i+\frac{1}{2}}, y, z, t)$ being a numerical flux function, which is obtained by solving the Riemann problem at an element interface, either exactly or approximately, at a generic time t . Equation (18) has been derived directly from the conservation equations and is an exact integral relation. In order to be used as a high order numerical one-step scheme in space and time, a number of actions must be taken, which are discussed in more detail in Sect. 3.2 and Sect. 3.3. The first one consists of a high order reconstruction of the solution within each control volume I_{ijk} , starting from the known cell averages $\bar{\mathbf{u}}_{ijk}^n$, which are the only quantities that are directly evolved in time via Eq. (18). Such a reconstruction of the conserved variables is performed through a high order weighted essentially non-oscillatory (WENO) interpolation, and provides a polynomial representation of the solution, as we will discuss below. In some cases, in order to reduce possible oscillations and to increase the accuracy, the reconstruction has been performed on the characteristic variables (Harten et al., 1987; Jiang and Shu, 1996) which are then transformed back to the conserved ones (Balsara, 2001; Toro, 2009). However, for challenging problems such as the one described in Sect. 4.4, the reconstruction (either in conserved or in characteristic variables) can cause failures when the conversion to the primitive variables is performed. Under these circumstances, it is advantageous to reduce the order of accuracy in the troubled cells, following the ”a-posteriori” MOOD strategy proposed by Clain et al. (2011) and applied here to the relativistic framework for the first time.

The second action required by our one-step time-update numerical scheme consists of computing, locally for each space-time cell C_{ijkn} , the time evolution of the reconstructed polynomial, which in the following we denote as $\mathbf{q}_h(x, y, z, t)$. This, in turns, allows to compute the solution of the Riemann problem at the cell interfaces as

$$\tilde{\mathbf{f}}_{\text{RP}} = \tilde{\mathbf{f}}(\mathbf{q}_h^-(x_{i+\frac{1}{2}}, y, z, t), \mathbf{q}_h^+(x_{i+\frac{1}{2}}, y, z, t)), \quad (23)$$

where \mathbf{q}_h^- and \mathbf{q}_h^+ are the left and right boundary extrapolated states at the interface, respectively. The form of the function $\tilde{\mathbf{f}}$ depends, of course, on the specific choice of the Riemann solver

adopted. Although exact Riemann solvers exist both for special relativistic hydrodynamics and magnetohydrodynamics (Martí and Müller, 1994; Rezzolla and Zanotti, 2001; Giacomazzo and Rezzolla, 2006), faster approximate Riemann solvers are typically preferred. In our calculations we have adopted two of them. The first one is the popular HLL Riemann solver by Harten et al. (1983), which does not rely on the characteristic structure of the equations and only needs the knowledge of the fastest and of the slowest of the eigenvalues. The second one is the Osher-type Riemann solver in the version proposed by Dumbser and Toro (2011) and it is based on the knowledge of the full spectral decomposition of the equations. Unlike the Roe Riemann solver, however, it is entropy-satisfying and thus does not produce unphysical rarefaction shocks. Because of the higher computational cost and complexity, we have used the Osher-type Riemann solver only for RHD systems, while for RMHD systems we have used the simpler HLL Riemann solver.

3.2. A dimension-by-dimension WENO reconstruction

The WENO reconstruction that we have implemented is genuinely multi-dimensional, but, from an operational point of view, it works in a dimension-by-dimension fashion. In practice, we first introduce spacetime reference coordinates $\xi, \eta, \zeta, \tau \in [0, 1]$, which are defined by

$$x = x_{i-\frac{1}{2}} + \xi \Delta x_i, \quad y = y_{j-\frac{1}{2}} + \eta \Delta y_j, \quad z = z_{k-\frac{1}{2}} + \zeta \Delta z_k, \quad t = t^n + \tau \Delta t. \quad (24)$$

After that, focusing on the x direction for convenience, we choose the degree M of the polynomial approximating the solution, and an orthogonal basis of polynomials (Solin, 2006), all of degree M , rescaled on the same unit interval $[0, 1]$. The basis is formed by the $M + 1$ Lagrange interpolation polynomials, $\{\psi_l(\lambda)\}_{l=1}^{M+1}$, passing through the $M + 1$ Gauss-Legendre quadrature nodes $\{\lambda_k\}_{k=1}^{M+1}$ and with the standard property that

$$\psi_l(\lambda_k) = \delta_{lk} \quad l, k = 1, 2, \dots, M + 1, \quad (25)$$

where δ_{lk} is the "Kronecker delta", i.e. $\delta_{lk} = 1$ if $l = k$, $\delta_{lk} = 0$ otherwise. Having done that, a (small) number of one-dimensional reconstruction stencils is adopted, each of them formed by the union of $M + 1$ adjacent cells, i.e.

$$\mathcal{S}_{ijk}^{s,x} = \bigcup_{e=i-L}^{i+R} I_{ejk}, \quad (26)$$

where $L = L(M, s)$ and $R = R(M, s)$ are the spatial extension of the stencil to the left and to the right. In practice, we have adopted the pragmatic approach for which odd order schemes (even polynomials of degree M) always use three stencils ($N_s = 3$), while even order schemes (odd polynomials of degree M) always adopt four stencils ($N_s = 4$), with the exception of the $M = 1$ case, for which there are only two stencils. For the sake of clarity, in Appendix A we have reported the coordinates of the Gaussian points, the nodal basis polynomials and the corresponding stencils for a few values of M up to $M = 4$.

With all this machinery at hands, we use the polynomial basis functions to reconstruct the solution at time t^n as⁴

$$\mathbf{w}_h^{s,x}(x, t^n) = \sum_{p=0}^M \psi_p(\xi) \hat{\mathbf{w}}_{ijk,p}^{n,s} := \psi_p(\xi) \hat{\mathbf{w}}_{ijk,p}^{n,s}, \quad (27)$$

⁴Note that here, and in the following, the Einstein summation convention is used over the repeated index p , even if such an index does not denote the covariant and contravariant components of a tensor.

As usual for finite volume methods, the reconstructed polynomial must preserve the cell-average of the solution over each element I_{ijk} , namely

$$\frac{1}{\Delta x_e} \int_{x_{e-\frac{1}{2}}}^{x_{e+\frac{1}{2}}} \psi_p(\xi(x)) \hat{\mathbf{w}}_{ijk,p}^{n,s} dx = \bar{\mathbf{u}}_{e,ijk}^n, \quad \forall I_{e,ijk} \in \mathcal{S}_{ijk}^{s,x}, \quad (28)$$

which provide a system of linear equations for the unknown coefficients $\hat{\mathbf{w}}_{ijk,p}^{n,s}$. This operation is repeated for each stencil relative to the element I_{ijk} . After that, we can construct a data-dependent nonlinear combination of the polynomials computed from each stencil, i.e.

$$\mathbf{w}_h^x(x, t^n) = \psi_p(\xi) \hat{\mathbf{w}}_{ijk,p}^n, \quad \text{with} \quad \hat{\mathbf{w}}_{ijk,p}^n = \sum_{s=1}^{N_s} \omega_s \hat{\mathbf{w}}_{ijk,p}^{n,s}. \quad (29)$$

The nonlinear weights ω_s are computed following the same logic as for the optimal WENO of Jiang and Shu (1996), i.e.

$$\omega_s = \frac{\tilde{\omega}_s}{\sum_k \tilde{\omega}_k}, \quad \tilde{\omega}_s = \frac{\lambda_s}{(\sigma_s + \epsilon)^r}. \quad (30)$$

However, the actual values of the linear weights λ_s are not the same as those of the optimal WENO and they are chosen according to a more pragmatic approach. In fact, the weight of the central stencils is given a very large value, $\lambda_s = 10^5$, while the weight of the one-sided stencils is set to $\lambda_s = 1$. Moreover, in our implementation we have used⁵ $\epsilon = 10^{-14}$ and $r = 8$. The oscillation indicator σ_s of Eq. (30) is

$$\sigma_s = \sum_{pm} \hat{\mathbf{w}}_{ijk,p}^{n,s} \hat{\mathbf{w}}_{ijk,m}^{n,s}, \quad (31)$$

and it requires the computation of the oscillation indicator matrix (Dumbser et al., 2008b)

$$\Sigma_{pm} = \sum_{\alpha=1}^M \int_0^1 \frac{\partial^\alpha \psi_p(\xi)}{\partial \xi^\alpha} \cdot \frac{\partial^\alpha \psi_m(\xi)}{\partial \xi^\alpha} d\xi, \quad (32)$$

which, compared to alternative expressions proposed in the literature, has the advantage that it does not depend on the grid spacing, and is therefore "universal". We emphasize that the reconstruction polynomial $\mathbf{w}_h^x(x, t^n)$ resulting from Eq. (29) is still an average in the y and z directions. Hence, the procedure explained so far is repeated along the two missing directions y and z . The net effect of this approach is to provide a genuine multidimensional reconstruction, although in such a way that each direction is treated separately.

3.3. The local space-time DG approach

The high order computation of the numerical fluxes (20)–(22), which contain a time integration from t^n to t^{n+1} , requires the numerical flux (Riemann solver) $\tilde{\mathbf{f}}_{\text{RP}}$ to be computed with high accuracy at any time in the interval $t \in [t^n; t^{n+1}]$. To this extent, we need an operation, to be

⁵It has been shown that the numerical results are substantially independent of ϵ and r (Liu et al., 1994).

performed locally for each cell, which uses as input the high order polynomial \mathbf{w}_h obtained from the WENO reconstruction, and gives as output its evolution in time, namely

$$\mathbf{w}_h(x, y, z, t^n) \longrightarrow \mathbf{q}_h(x, y, z, t). \quad (33)$$

Unlike the original ADER approach, where this operation was obtained through the so called Cauchy-Kovalewski procedure (Toro and Titarev, 2005; Dumbser et al., 2007), in the modern version of ADER the transformation represented by (33) is obtained through an element–local space–time Discontinuous Galerkin predictor that is based on the *weak* integral form of Eq. (7) (Dumbser et al., 2008b). The basic idea can be summarized as follows. The sought polynomial $\mathbf{q}_h(x, y, z, t)$ is supposed to be expanded in space and time as

$$\mathbf{q}_h = \mathbf{q}_h(\xi, \tau) = \theta_p(\xi, \tau) \hat{\mathbf{q}}_p, \quad (34)$$

where the polynomial basis functions θ_p are given by a tensor–product of the basis functions ψ_l already used for the WENO reconstruction, namely

$$\theta_p(\xi, \tau) = \psi_p(\xi)\psi_q(\eta)\psi_r(\zeta)\psi_s(\tau). \quad (35)$$

The terms $\hat{\mathbf{q}}_p$ are the so-called degrees of freedom and they are the unknowns of the problem. After multiplying the governing PDE of Eq. (7), written in the reference coordinates (ξ, η, ζ, τ) , with the space–time test functions θ_q and integrating over the space–time reference control volume, we obtain⁶

$$\int_0^1 \int_0^1 \int_0^1 \int_0^1 \theta_q \left(\frac{\partial \mathbf{u}}{\partial \tau} + \frac{\partial \mathbf{f}^*}{\partial \xi} + \frac{\partial \mathbf{g}^*}{\partial \eta} + \frac{\partial \mathbf{h}^*}{\partial \zeta} \right) d\xi d\eta d\zeta d\tau = 0. \quad (37)$$

The key aspect of the whole strategy is to perform an integration by parts in time, while keeping the treatment local in space. After doing so, we get

$$\begin{aligned} & \int_0^1 \int_0^1 \int_0^1 \theta_q(\xi, 1) \mathbf{u}(\xi, 1) d\xi d\eta d\zeta - \int_0^1 \int_0^1 \int_0^1 \int_0^1 \left(\frac{\partial}{\partial \tau} \theta_q \right) \mathbf{u} d\xi d\eta d\zeta d\tau \\ & + \int_0^1 \int_0^1 \int_0^1 \int_0^1 \left[\theta_q \left(\frac{\partial \mathbf{f}^*}{\partial \xi} + \frac{\partial \mathbf{g}^*}{\partial \eta} + \frac{\partial \mathbf{h}^*}{\partial \zeta} \right) \right] d\xi d\eta d\zeta d\tau = \int_0^1 \int_0^1 \int_0^1 \theta_q(\xi, 0) \mathbf{u}(\xi, t^n) d\xi d\eta d\zeta \end{aligned} \quad (38)$$

In the first two integrands of Eq. (38) we can perform the replacement $\mathbf{u} \rightarrow \mathbf{q}_h$, since \mathbf{q}_h is the discrete space-time solution we are looking for. In the integrand on the right hand side of Eq. (38), on the other hand, we can perform the replacement $\mathbf{u}(\xi, t^n) \rightarrow \mathbf{w}_h(\xi, t^n)$, since at time t^n the solution is known, and it is represented by the reconstructed polynomial computed according to the procedure described in Sect. 3.2. In addition to this, we assume that the fluxes too can be expanded over the basis as we did in Eq. (34), namely

$$\mathbf{f}_h^* = \theta_p \hat{\mathbf{f}}_p^*, \quad \mathbf{g}_h^* = \theta_p \hat{\mathbf{g}}_p^*, \quad \mathbf{h}_h^* = \theta_p \hat{\mathbf{h}}_p^*. \quad (39)$$

⁶Here we have defined

$$\mathbf{f}^* = \frac{\Delta t}{\Delta x_i} \mathbf{f}, \quad \mathbf{g}^* = \frac{\Delta t}{\Delta y_j} \mathbf{g}, \quad \mathbf{h}^* = \frac{\Delta t}{\Delta z_k} \mathbf{h}. \quad (36)$$

From the computational point of view, the advantage of the nodal basis becomes apparent at this stage. In fact, the above degrees of freedom for the fluxes are simply the point-wise evaluation of the physical fluxes, hence

$$\hat{\mathbf{f}}_p^* = \mathbf{f}^*(\hat{\mathbf{q}}_p), \quad \hat{\mathbf{g}}_p^* = \mathbf{g}^*(\hat{\mathbf{q}}_p), \quad \hat{\mathbf{h}}_p^* = \mathbf{h}^*(\hat{\mathbf{q}}_p). \quad (40)$$

Had a modal basis been adopted instead, $\hat{\mathbf{f}}_p^*$, $\hat{\mathbf{g}}_p^*$ and $\hat{\mathbf{h}}_p^*$ could have been obtained only after performing a time-consuming ‘‘L2-projection’’. Inserting Eqns. (34) and (39) into (38) yields

$$\begin{aligned} & \int_0^1 \int_0^1 \int_0^1 \theta_q(\xi, 1) \theta_p(\xi, 1) \hat{\mathbf{q}}_p \, d\xi d\eta d\zeta - \int_0^1 \int_0^1 \int_0^1 \int_0^1 \left(\frac{\partial}{\partial \tau} \theta_q \right) \theta_p \hat{\mathbf{q}}_p \, d\xi d\eta d\zeta d\tau \\ & + \int_0^1 \int_0^1 \int_0^1 \int_0^1 \left[\theta_q \left(\frac{\partial}{\partial \xi} \theta_p \hat{\mathbf{f}}_p^* + \frac{\partial}{\partial \eta} \theta_p \hat{\mathbf{g}}_p^* + \frac{\partial}{\partial \zeta} \theta_p \hat{\mathbf{h}}_p^* \right) \right] d\xi d\eta d\zeta d\tau \\ & = \int_0^1 \int_0^1 \int_0^1 \theta_q(\xi, 0) \mathbf{w}_h(\xi, t^n) \, d\xi d\eta d\zeta. \end{aligned} \quad (41)$$

It may be noticed that Eq. (41) contains several integrals which only involve the basis functions and their derivatives, and which can be pre-computed in the code. Hence, after defining the integrals

$$\mathbf{K}_{qp}^1 = \int_0^1 \int_0^1 \int_0^1 \theta_q(\xi, 1) \theta_p(\xi, 1) d\xi - \int_0^1 \int_0^1 \int_0^1 \int_0^1 \left(\frac{\partial}{\partial \tau} \theta_q \right) \theta_p d\xi d\tau, \quad (42)$$

$$\mathbf{K}_{qp}^\xi = (\mathbf{K}_{qp}^\xi, \mathbf{K}_{qp}^\eta, \mathbf{K}_{qp}^\zeta) = \int_0^1 \int_0^1 \int_0^1 \int_0^1 \theta_q \frac{\partial}{\partial \xi} \theta_p d\xi d\tau, \quad (43)$$

$$\mathbf{F}_{qp}^0 = \int_0^1 \int_0^1 \int_0^1 \theta_q(\xi, 0) \psi_m(\xi) d\xi, \quad (44)$$

where $d\xi = d\xi d\eta d\zeta$, we can rewrite the system (41) in a compact form as an algebraic equation system for the unknown coefficients $\hat{\mathbf{q}}_p$, i.e.

$$\mathbf{K}_{qp}^1 \hat{\mathbf{q}}_p + \mathbf{K}_{qp}^\xi \cdot \hat{\mathbf{f}}_p^* + \mathbf{K}_{qp}^\eta \hat{\mathbf{g}}_p^* + \mathbf{K}_{qp}^\zeta \hat{\mathbf{h}}_p^* = \mathbf{F}_{qm}^0 \hat{\mathbf{w}}_m^n. \quad (45)$$

This system of equations must be solved approximately through standard iterative procedures up to a desired tolerance, and it represents the single most expensive routine in a typical simulation, amounting to $\sim [24 - 28]\%$ of the total CPU time. It is also interesting to note that the ADER approach becomes particularly convenient in case of relativistic hydrodynamics. In fact, by avoiding the sub-steps typical of Runge–Kutta schemes, it avoids the conversion from conserved to primitive variables that would be required at each sub-step, and that is always a delicate and time-consuming operation. Again in a typical simulation, the CPU time spent in the conversion from the conserved to the primitive variables is $\sim [12 - 16]\%$ of the total CPU time.

The proposed approach has been shown to cope successfully even with stiff source terms (Dumbser and Zanotti, 2009; Zanotti and Dumbser, 2011). However, there is no such a necessity in the case of special relativistic hydrodynamics, whose source terms vanish in Cartesian coordinates.

3.4. Adaptive mesh refinement

AMR algorithms can be roughly divided in two main categories. In the first category, nested arrays of logically rectangular grid patches are used, according to the original Berger-Colella-Oliger approach (Berger and Oliger, 1984; Berger and Colella, 1989). In the second category, a 'cell-by-cell' refinement is instead adopted, and the resulting cells are managed as elements of a tree-data structure. It is in this version that AMR techniques were first applied to astrophysics, for performing N-body cosmological simulations (Khokhlov et al., 1997), and this is also the strategy that we have implemented. We refer to Dumbser et al. (2013) for a detailed description of our AMR algorithm, which was extensively validated for the classical Euler and magneto-hydrodynamics equations. We just recall here that, as in any other AMR algorithm, there are a number of free parameters, namely

- The maximum level of refinement ℓ_{\max} , typically 2 or 3 in our tests.
- The refinement factor τ , governing the number of sub-cells that are generated according to

$$\Delta x_\ell = \tau \Delta x_{\ell+1} \quad \Delta y_\ell = \tau \Delta y_{\ell+1} \quad \Delta z_\ell = \tau \Delta z_{\ell+1}, \quad (46)$$

where Δx_ℓ is size of the cell, at ℓ refinement level, along the x -direction, and similarly for the other directions.

- The choice of the refinement criterion, which in our approach is simply feature-based, uses the calculation of a second derivative, see Löhner (1987). In practice, a cell C_m is marked for refinement if $\chi_m > \chi_{\text{ref}}$, while it is marked for re-coarsening if $\chi_m < \chi_{\text{rec}}$, where

$$\chi_m = \sqrt{\frac{\sum_{k,l} (\partial^2 \Phi / \partial x_k \partial x_l)^2}{\sum_{k,l} [(|\partial \Phi / \partial x_k|_{i+1} + |\partial \Phi / \partial x_k|_i) / \Delta x_l + \varepsilon |(\partial^2 / \partial x_k \partial x_l)| |\Phi|]}]} \cdot \quad (47)$$

The summation $\sum_{k,l}$ is taken over the number of space dimension of the problem in order to include the cross term derivatives. The function $\Phi = \Phi(\mathbf{u})$ can be any suitable indicator function of the conserved variables \mathbf{u} and in all our tests we have used $\Phi(\mathbf{u}) = D = \rho W$. We have observed that the threshold values χ_{ref} and χ_{rec} can be slightly model dependent. In most of our tests we have chosen χ_{ref} in the range $\sim [0.2, 0.25]$ and χ_{rec} in the range $\sim [0.05, 0.15]$. Moreover, the first and second derivatives involved in the definition of χ_m are computed through standard finite-differencing based on the cell averages of \mathbf{u} . Finally, the parameter ε acts as a filter preventing refinement in regions of small ripples and is given the value $\varepsilon = 0.01$. In alternative, we refer the reader to the use of error based adaptation as investigated by Baeza et al. (2012) in the context of the high order WENO AMR schemes first proposed by Baeza and Mulet (2006).

4. Numerical tests

In this Section we consider a wide set of numerical test cases, both for RHD systems, discussed in Sect. 4.1–4.7, and for RMHD systems, discussed in Sect. 4.8–4.11. The analysis of the order of convergence is deferred to Sect. 4.8.

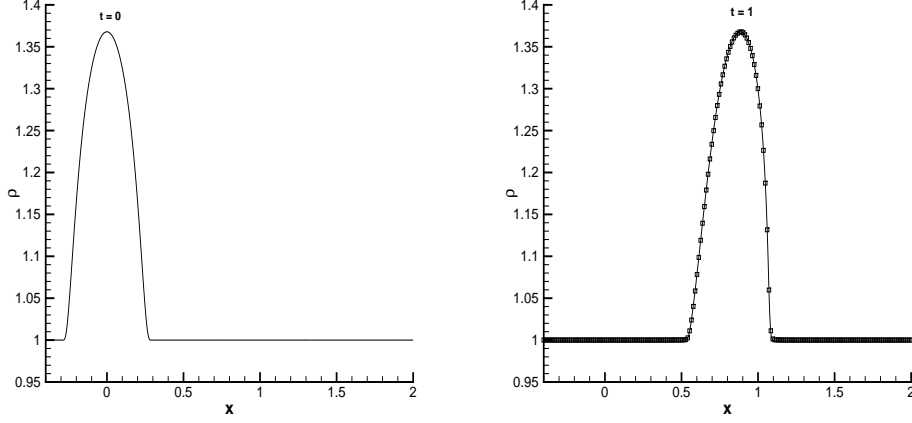


Figure 1: Isentropic one-dimensional flow. Left panel: initial profile of the rest-mass density. Right panel: solution at time $t = 1.0$ obtained with the fourth order ADER-WENO scheme.

4.1. RHD one-dimensional isentropic flow

The first test that we have considered, already studied by Zhang and MacFadyen (2006) and Radice and Rezzolla (2012), describes a one-dimensional simple wave (Anile, 1990), namely a smooth solution for which two, out of the three, Riemann invariants associated to the acoustic eigenvalues are constant. Such Riemann invariants are the specific entropy s and one of the two quantities

$$J_{\pm} = \frac{1}{2} \ln \left(\frac{1+v}{1-v} \right) \pm \frac{1}{\sqrt{\gamma-1}} \ln \left(\frac{\sqrt{\gamma-1} + c_s}{\sqrt{\gamma-1} - c_s} \right), \quad (48)$$

where the sound speed c_s is given by

$$c_s^2 = \frac{\gamma p}{h \rho} = \frac{\gamma(\gamma-1)p}{\gamma p + (\gamma-1)\rho}. \quad (49)$$

In our calculations, we have chosen J_- as constant, hence describing an isentropic right-propagating simple wave (Anile et al., 1983). Consistently with these assumptions, the fluid obeys a poly-tropic equation of state of the type

$$p = K \rho^\gamma. \quad (50)$$

The initial profile of the rest-mass density is chosen as in Radice and Rezzolla (2012), i.e.

$$\rho(x, 0) = \begin{cases} 1 + \exp[-1/(1-x^2/L^2)] & \text{for } |x| < L, \\ 1 & \text{for } |x| > L, \end{cases} \quad (51)$$

where L determines the width of the profile. Since $\rho(x, 0) = 1$ and $v(x, 0) = 0$ for $|x| > L$, Eq. (48) can be used to compute the value of J_- and, consequently, the profile of the initial velocity in the range $-L < x < L$. As the wave propagates towards the right, steepening occurs until a shock

Table 1: Initial left (L) and right (R) states of the relativistic shock tube problems. The last two columns report the adiabatic index and the final time t_f of the simulation.

Problem	ρ_L	v_L	p_L	ρ_R	v_R	p_R	γ	t_f
1	1	-0.6	10	10	0.5	20	5/3	0.4
2	10^{-3}	0	1	10^{-3}	0	10^{-5}	5/3	0.4
3	1	0.9	1	1	0	10	4/3	0.4

wave forms. In our calculations we have solved the problem over the computational domain $-0.4 < x < 2.0$ up to time $t = 1.0$ (before the shock formation) and we have used $K = 100$, $\gamma = 5/3$, $L = 0.3$.

Fig.1 shows the results of our calculation for the representative model with 40 cells on the level zero grid (see Tab. 3), for which a fourth order ADER-WENO scheme with $\ell_{\max} = 2$ and $\tau = 3$ have been adopted. The left panel reports the initial condition, while the right panel depicts the solution at the final time, compared to the reference solution.

4.2. RHD one-dimensional Riemann problems

To further validate the new scheme, we have considered a set of relativistic shock tubes, with initial conditions reported in Table 1. In all cases the numerical solution has been computed both with the HLL and with the Osher-type Riemann solver, and has been compared to the exact solution computed according to the procedure outlined in Rezzolla and Zanotti (2001). In the three tests analyzed below the numerical domain $[0, 1]$ is covered by an initial uniform mesh composed of 100 cells.

Problem 1, considered also by Mignone and Bodo (2005), has initial conditions producing a wave-pattern that consists of two rarefaction waves (henceforth, a $2\mathcal{R}$ wave-pattern), propagating to the left and to the right, and the usual contact discontinuity between them. A fourth order WENO scheme with $\ell_{\max} = 2$, $\tau = 3$ and CFL = 0.6 has been used. The results of this test are shown in Fig. 2, with HLL and Osher fluxes reproducing the exact solution with essentially the same accuracy.

Problem 2, considered also by Radice and Rezzolla (2012), has initial conditions producing a wave-pattern that consists of a rarefaction wave, propagating to the left, a contact discontinuity and a shock wave propagating to the right (henceforth, a \mathcal{RS} wave-pattern). The shock wave is characterized by a strong density contrast. A fourth order WENO scheme with $\ell_{\max} = 2$, $\tau = 3$ and CFL = 0.6 has been used. The results of this test are shown in Fig. 3. We note that in this case the Osher flux gives a slightly better representation of the blast wave, as can be seen from the inset in the central panel.

Problem 3, considered also by Zhang and MacFadyen (2006), has initial conditions producing a wave-pattern that consists of two shock waves, propagating to the left and to the right, plus again the contact discontinuity between them (henceforth, a $2\mathcal{S}$ wave-pattern). A fourth order WENO scheme with $\ell_{\max} = 2$, $\tau = 3$ and CFL = 0.6 has been used. The results of this test are shown in Fig. 4. We note that some oscillations appear in the post-shock region of the right-propagating shock, which are particularly visible in the rest mass density and in the pressure. Such oscillations are stronger for the Osher flux than for the more dissipative HLL flux.

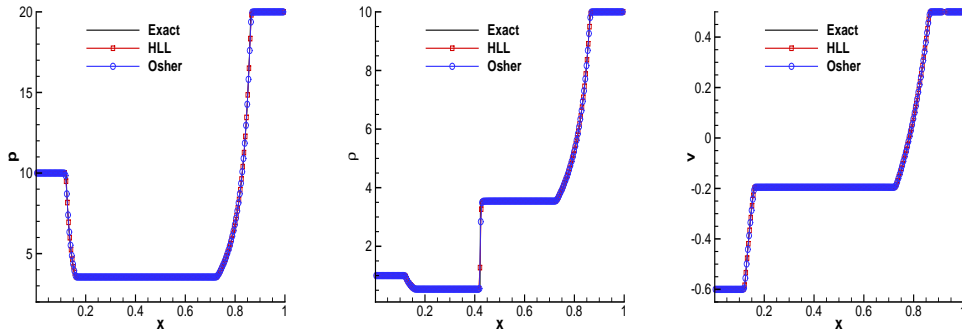


Figure 2: Solution of Problem 1 (see Table 1) with the fourth order ADER-WENO scheme at time $t = 0.4$.

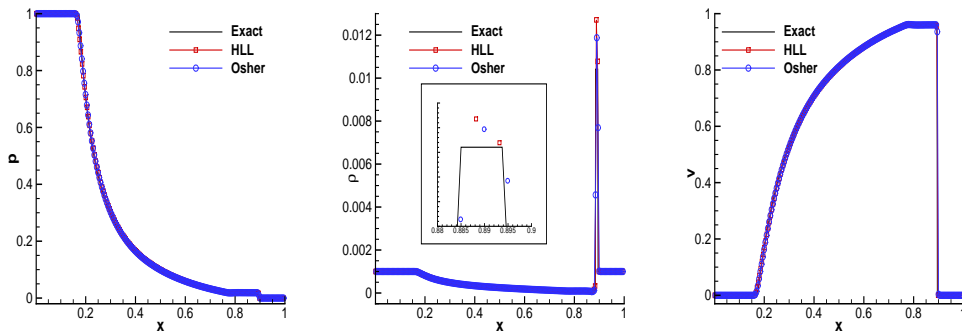


Figure 3: Solution of Problem 2 (see Table 1) with the fourth order ADER-WENO scheme at time $t = 0.4$.

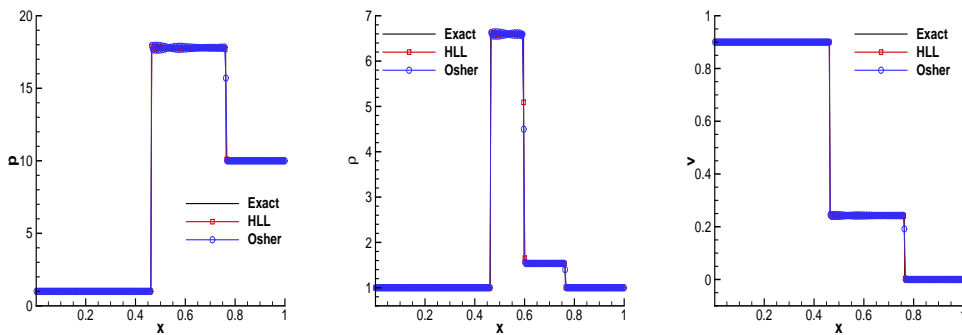


Figure 4: Solution of Problem 3 (see Table 1) with the fourth order ADER-WENO scheme at time $t = 0.4$.

Table 2: Numerical convergence results for the shock tube problems using the second, the third and the fourth order version of the scheme. The error L_2 -norms refer to the variable ρ (density) at the final time $t_f = 0.4$.

$\ell_{\max} = 0$, Problem 1						
N_G	ϵ_{L_2}	$\mathcal{O}(L_2)$	ϵ_{L_2}	$\mathcal{O}(L_2)$	ϵ_{L_2}	$\mathcal{O}(L_2)$
	$\mathcal{O}2$	$\mathcal{O}2$	$\mathcal{O}3$	$\mathcal{O}3$	$\mathcal{O}4$	$\mathcal{O}4$
48	0.1040E+0		8.1633E-02		8.0836E-02	
96	7.2390E-02	0.52	5.0825E-02	0.68	4.8533E-02	0.73
192	4.9323E-02	0.55	3.6793E-02	0.46	3.2851E-02	0.56
288	3.9808E-02	0.53	2.8863E-02	0.60	2.6741E-02	0.51
384	3.4400E-02	0.51	2.6361E-02	0.31	2.3341E-02	0.47
$\ell_{\max} = 0$, Problem 2						
N_G	ϵ_{L_2}	$\mathcal{O}(L_2)$	ϵ_{L_2}	$\mathcal{O}(L_2)$	ϵ_{L_2}	$\mathcal{O}(L_2)$
	$\mathcal{O}2$	$\mathcal{O}2$	$\mathcal{O}3$	$\mathcal{O}3$	$\mathcal{O}4$	$\mathcal{O}4$
48	2.3516E-04		2.7214E-04		2.1798E-04	
96	2.2984E-04	0.03	2.3015E-04	0.24	1.9878E-04	0.13
192	2.2027E-04	0.06	1.8076E-04	0.35	1.6360E-04	0.28
288	2.0329E-04	0.19	1.5462E-04	0.38	1.4305E-04	0.33
384	1.8807E-04	0.27	1.3605E-04	0.44	1.2920E-04	0.35
$\ell_{\max} = 0$, Problem 3						
N_G	ϵ_{L_2}	$\mathcal{O}(L_2)$	ϵ_{L_2}	$\mathcal{O}(L_2)$	ϵ_{L_2}	$\mathcal{O}(L_2)$
	$\mathcal{O}2$	$\mathcal{O}2$	$\mathcal{O}3$	$\mathcal{O}3$	$\mathcal{O}4$	$\mathcal{O}4$
48	0.1375E-00		0.1084E-00		9.8280E-02	
96	9.0721E-02	0.60	7.6012E-02	0.51	7.9195E-02	0.31
192	6.0782E-02	0.58	5.2709E-02	0.53	5.1727E-02	0.61
288	6.0567E-02	0.01	4.9566E-02	0.15	5.1590E-02	0.01
384	4.9106E-02	0.73	4.3106E-02	0.48	3.8403E-02	1.03
$\ell_{\max} = 2$, Problem 1						
N_G	ϵ_{L_2}	$\mathcal{O}(L_2)$	ϵ_{L_2}	$\mathcal{O}(L_2)$	ϵ_{L_2}	$\mathcal{O}(L_2)$
		$\mathcal{O}2$		$\mathcal{O}3$		$\mathcal{O}4$
50	3.2766E-02		2.5525E-02		2.2031E-02	
100	2.4211E-02	0.43	1.7979E-02	0.50	1.5174E-02	0.54
150	2.0189E-02	0.45	1.4871E-02	0.47	1.3248E-02	0.33
200	1.7895E-02	0.42	1.2979E-02	0.47	1.1311E-02	0.54
250	1.6391E-02	0.39	1.2376E-02	0.21	1.0004E-02	0.55
$\ell_{\max} = 2$, Problem 2						
N_G	ϵ_{L_2}	$\mathcal{O}(L_2)$	ϵ_{L_2}	$\mathcal{O}(L_2)$	ϵ_{L_2}	$\mathcal{O}(L_2)$
		$\mathcal{O}2$		$\mathcal{O}3$		$\mathcal{O}4$
50*	1.8277E-04		1.3901E-04		1.3543E-04	
100	1.3735E-04	0.41	9.1050E-05	0.61	8.4308E-05	0.68
150	1.1605E-04	0.41	7.6561E-05	0.43	6.9318E-05	0.43
200	1.0367E-04	0.39	6.9863E-05	0.32	5.8261E-05	0.60
250	9.5207E-05	0.38	6.0027E-05	0.68	5.1095E-05	0.59
$\ell_{\max} = 2$, Problem 3						
N_G	ϵ_{L_2}	$\mathcal{O}(L_2)$	ϵ_{L_2}	$\mathcal{O}(L_2)$	ϵ_{L_2}	$\mathcal{O}(L_2)$
		$\mathcal{O}2$		$\mathcal{O}3$		$\mathcal{O}4$
50*	5.0893E-02		4.1120E-02		4.1825E-02	
100	3.6623E-02	0.47	2.9813E-02	0.46	2.7244E-02	0.62
150	2.9965E-02	0.49	2.7059E-02	0.24	2.3018E-02	0.41
200	2.9446E-02	0.06	2.4190E-02	0.39	2.0958E-02	0.32
250	2.5318E-02	0.67	1.9509E-02	0.96	1.6690E-02	1.02

Table 2 reports an analysis of the L_2 norms of the error (computed with respect to the available exact solution) and the corresponding orders of convergence. This analysis has been performed with the Osher flux and with reconstruction in characteristic variables, for both the cases $\ell_{\max} = 0$ (no AMR) and $\ell_{\max} = 2$. As expected for solutions with discontinuities, the order of convergence is usually smaller or equal to unity. In a few cases, e.g. for Problem 2 with $\ell_{\max} = 0$ and $N_G = 96$, the convergence is anomalously low and very closed to zero. This typically happens when there are a few cells manifesting oscillations at discontinuities. Moreover, the absolute value of the error decreases as the nominal order of the scheme is increased.

4.3. RHD one-dimensional Riemann problems with tangential velocities

In spite of the obvious additional complications introduced by special relativity, the one-dimensional Riemann problem without tangential velocities does not introduce qualitative differences with respect to its Newtonian analog. The situation changes drastically when tangential velocities are present.⁷ As shown by Rezzolla and Zanotti (2002), the coupling of the velocity components through the Lorentz factor is responsible of a new effect which is not present in Newtonian hydrodynamics. Namely, given a Riemann problem with initial conditions producing a \mathcal{RS} wave pattern and a non zero relative velocity along the normal direction, it is always possible to transform it into a $2\mathcal{S}$ wave-pattern by increasing the value of the initial tangential velocity in the state of initial *lower* pressure, while keeping the rest of the variables unmodified. Similarly, given a Riemann problem with initial conditions producing a \mathcal{RS} wave pattern and a non zero relative velocity along the normal direction, it is always possible to transform it into a $2\mathcal{R}$ wave-pattern by increasing the value of the initial tangential velocity in the state of initial *higher* pressure. Besides being at the heart of a possible acceleration mechanism in relativistic jets (Aloy and Rezzolla, 2006), this physical effect is also interesting from a numerical point of view, since it can be used to test the ability of a relativistic code in treating dynamical systems with fully coupled velocities.

We have simulated one such relevant example that has the following initial conditions

$$(\rho, v_x, v_t, p) = \begin{cases} (1.0, 0.8, 0.0, 1000.0) & \text{for } x < 0.5, \\ (1.0, 0.0, 0.999, 0.01) & \text{for } x > 0.5, \end{cases} \quad (52)$$

and adiabatic index $\gamma = 5/3$. In the absence of tangential velocities, namely when $v_t = 0$ on both initial states, the solution to this Riemann problem would consist of a \mathcal{RS} wave-pattern. However, due to the high value of v_t on the right state, the wave-pattern changes to a $2\mathcal{S}$ one. The solution is reported in Fig. 5, which also shows the reference solution computed according to Rezzolla et al. (2003). A third order WENO scheme with $\ell_{\max} = 2$, $\tau = 3$ and CFL = 0.6 has been used, proving the ability of the code in treating configurations with highly coupled velocity components. We note that for this test the HLL and the Osher-type Riemann solver provides essentially the same accuracy and only the data obtained with HLL have been plotted in the figure.

4.4. RHD two-dimensional Riemann problem

In the first of our multi-dimensional tests we solve the two-dimensional Riemann problem originally proposed by Del Zanna and Bucciantini (2002), and later reproduced by Lucas-Serrano et al.

⁷ A velocity component is tangential if it belongs to the plane normal to the discontinuity front.

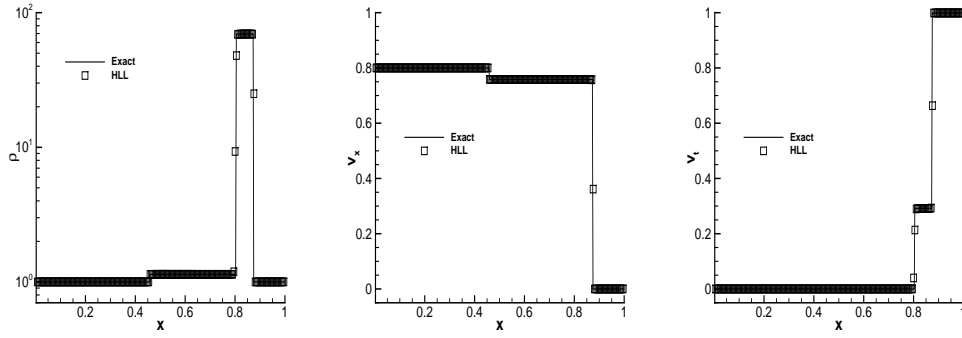


Figure 5: Solution of the Riemann problem with a non-zero tangential velocity at time $t = 0.4$. A third order ADER-WENO scheme has been used.

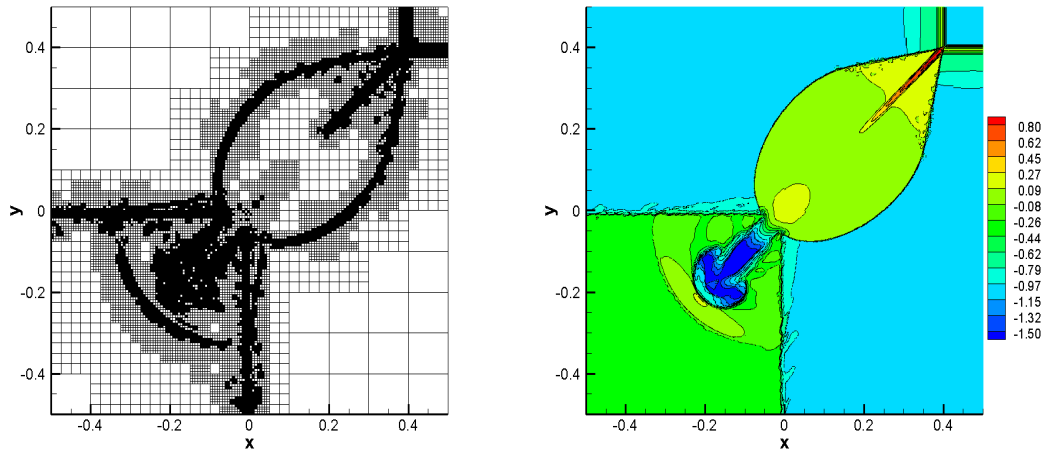


Figure 6: Solution of the 2D Riemann Problem obtained with a third order ADER-WENO scheme at time $t = 0.4$. Left panel: snapshot of the AMR grid. Right panel: logarithm of the rest mass density.

(2004), Mignone and Bodo (2005), Zhang and MacFadyen (2006). We emphasize that in this problem the order of accuracy is the third, corresponding to $M = 2$, essentially motivated by the necessity to reduce the computational time due to the constraint $\tau \geq M$ required by our scheme. The initial conditions are prescribed over the square $[-1, 1] \times [-1, 1]$ and are given by

$$(\rho, v_x, v_y, p) = \begin{cases} (0.1, 0.99, 0, 1) & \text{for } x < 0, y > 0, \\ (0.1, 0, 0, 0.01) & \text{for } x > 0, y > 0, \\ (0.5, 0, 0, 1) & \text{for } x < 0, y < 0, \\ (0.1, 0, 0.99, 1) & \text{for } x > 0, y < 0, \end{cases} \quad (53)$$

with adiabatic index $\gamma = 5/3$. As the system evolves in time, two curved shock fronts propagate in the upper-right quadrant, while a jet-like structure emerges along the main diagonal. We have solved this problem with a third order WENO scheme applied to the characteristic variables and using the HLL Riemann solver. The grid is initially uniform with 20×20 cells. Three levels of refinement have been adopted, with $\tau = 4$ and $\text{CFL} = 0.4$. The results of our computations are reported in Fig.6, which shows the contour-plot of the rest mass density (right panel) and the corresponding AMR grid (left panel) at the final time $t = 0.4$. We stress that, in a limited number of troubled cells close to the corner $(0, 0)$, the accuracy of the solution has been intentionally reduced to first-order following a MOOD-type approach [see Clain et al. (2011)], to avoid the appearance of strong oscillations which make the recovering of the primitive variables fail. In spite of this, the solution is very well reproduced by our numerical scheme and it can be compared with that obtained by Lucas-Serrano et al. (2004) using the same order of accuracy on a uniform mesh composed of 400×400 elements.

4.5. RHD Kelvin–Helmholtz instability

The Kelvin–Helmholtz (KH) instability is a classical instability of fluid dynamics and in the astrophysical context is currently invoked to explain the observed phenomenology of extended radio-jets [see Martí and Müller (2003) and references therein]. In this section we present a simple test performed in two dimensions, where the linear growth phase of the KH instability is reproduced. Following the works of Mignone et al. (2009), Beckwith and Stone (2011) and Radice and Rezzolla (2012), we choose the initial conditions as

$$v_x = \begin{cases} v_s \tanh [(y - 0.5)/a] & y > 0, \\ -v_s \tanh [(y + 0.5)/a] & y \leq 0, \end{cases} \quad (54)$$

where $v_s = 0.5$ is the velocity of the shear layer and $a = 0.01$ is its characteristic size. In order to trigger the instability, a perturbation in the transverse velocity is introduced as

$$v_y = \begin{cases} \eta_0 v_s \sin (2\pi x) \exp [-(y - 0.5)^2/\sigma] & y > 0, \\ -\eta_0 v_s \sin (2\pi x) \exp [-(y + 0.5)^2/\sigma] & y \leq 0, \end{cases} \quad (55)$$

where $\eta_0 = 0.1$ is the amplitude of the perturbation, while $\sigma = 0.1$ is its length scale. Finally, the rest-mass density is chosen as

$$\rho = \begin{cases} \rho_0 + \rho_1 \tanh [(y - 0.5)/a] & y > 0, \\ \rho_0 - \rho_1 \tanh [(y + 0.5)/a] & y \leq 0, \end{cases} \quad (56)$$

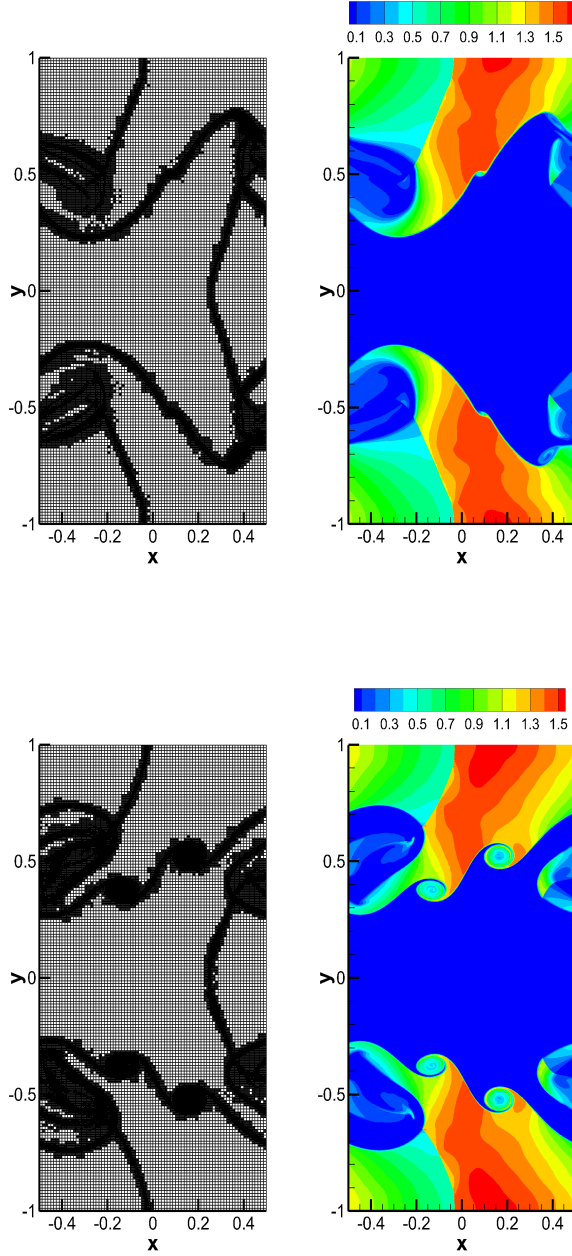


Figure 7: Two-dimensional Kelvin-Helmholtz instability at $t = 3.0$ with **refinement factor $\tau = 3$** . Left panels: the AMR grid. Right panels: the distribution of the rest-mass density. Top panels: results obtained with the HLL Riemann solver. Bottom panels: results obtained with the Osher Riemann solver. In both cases a third order ADER-WENO with CFL=0.4 has been adopted.

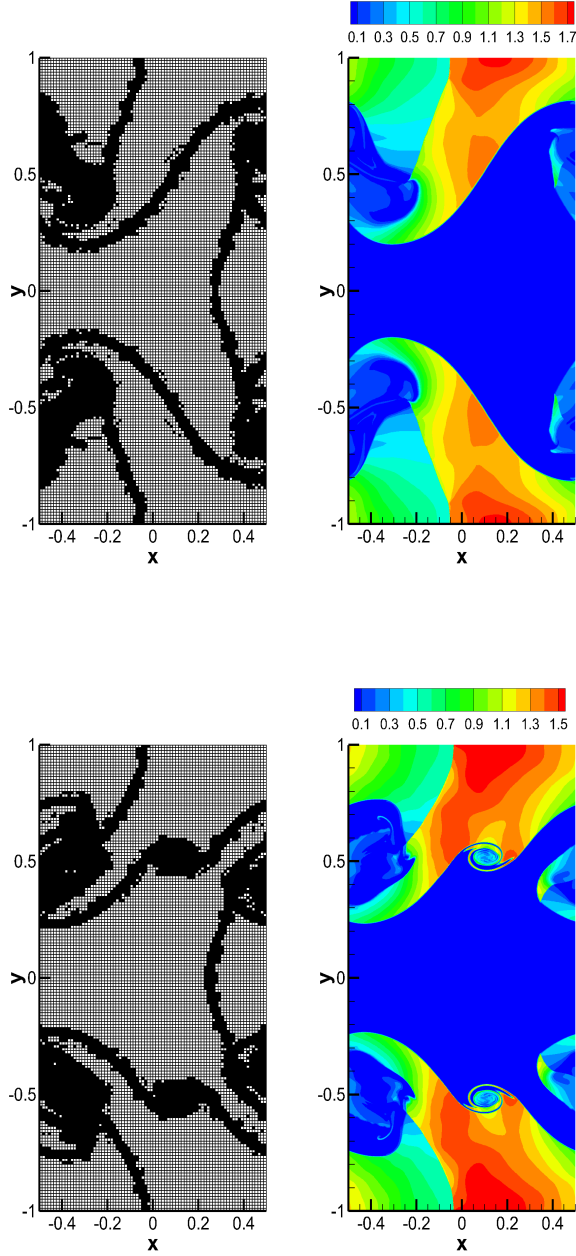


Figure 8: Two-dimensional Kelvin-Helmholtz instability at $t = 3.0$ with **refinement factor** $\tau = 4$. Left panels: the AMR grid. Right panels: the distribution of the rest-mass density. Top panels: results obtained with the HLL Riemann solver. Bottom panels: results obtained with the Osher Riemann solver. In both cases a third order ADER-WENO with CFL=0.4 has been adopted.

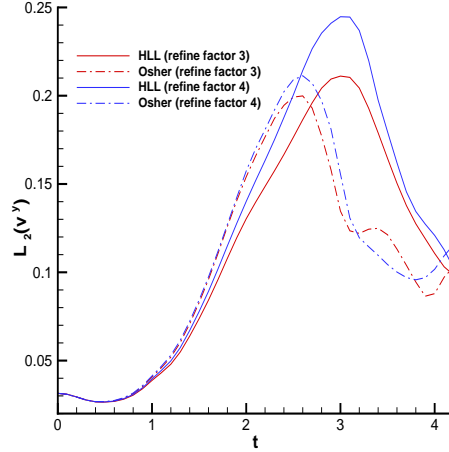


Figure 9: Time evolution of the L_2 norm of v_y , showing the transition from the linear to the non-linear phase of the KH instability, occurring for $t \in [2, 3]$. The red and blue curves refer to the refinement factor $\tau = 3$ and $\tau = 4$, respectively. The comparison between HLL and Osher is also shown.

with $\rho_0 = 0.505$ and $\rho_1 = 0.495$. The adiabatic index is $\gamma = 4/3$ and the pressure is $p = 1$ everywhere.

We have solved this problem on a rectangular domain $[-0.5, 0.5] \times [-1, 1]$, starting from an initial uniform grid with resolution 80×160 and adopting periodic boundary conditions both in x and in y directions. A third order ADER-WENO has been chosen and AMR is activated with relevant parameters $\ell_{\max} = 2$ and $\text{CFL}=0.4$. The results of our computations are reported in Fig. 7 and in Fig. 8, which refer to a refinement factor $\tau = 3$ and $\tau = 4$, respectively. In each figure the left panels display the AMR grid at time $t = 3$ while the right panels display the corresponding distribution of the rest-mass density. Finally, the top and the bottom panels refer to the HLL Riemann solver and to the Osher-type Riemann solver, respectively. In all cases we have performed reconstruction on the characteristic variables. At least two comments can be made about these results. First, the more diffusive HLL Riemann solver does not allow for the development of secondary small-scale instabilities along the shear layer (compare the top and the bottom panels in each figure). Second, although the Osher-type Riemann solver is clearly able to capture the formation of tiny structures, by increasing the resolution the number of produced vortices decreases. This is evident after comparing the bottom panels of Fig. 7 and Fig. 8 which, at the reported time $t = 3$, have 269,858 and 627,024 cell elements, respectively. This result suggests that these secondary instabilities do not have a clear physical origin, and confirms what already found by Radice and Rezzolla (2012).

The growth scale of the instability is instead shown in Fig. 9, where we have plotted, as a function of time, the L_2 norm of the transverse velocity v_y . This is in fact a global quantity suitable to monitor the development of the instability. The red and the blue curves refer to the refinement factor $\tau = 3$ and $\tau = 4$, respectively, while the continuous and the dashed lines are used to distinguish among the two Riemann solvers adopted. The transition from the linear to

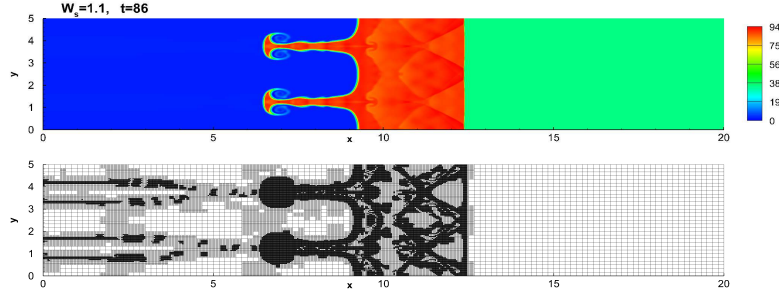


Figure 10: Third order simulation of the RM instability in a configuration with Lorentz factor $W_s = 1.1$. The instability is fully developed. Only a portion of the numerical grid is shown.

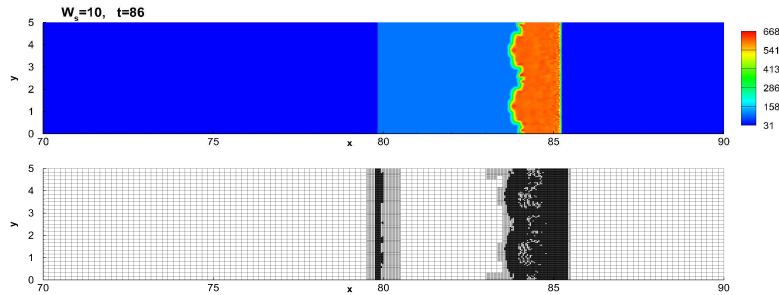


Figure 11: Third order simulation RM instability in a configuration with Lorentz factor $W_s = 10$. The instability is essentially suppressed. Only a portion of the numerical grid is shown.

the non-linear regime occurs for $t \in [2, 3]$ and it is slightly delayed when the diffusive HLL solver is used. Moreover, in the higher resolution simulations obtained with $\tau = 4$, the steepness of the linear phase is larger, producing higher maxima of $L_2(v_y)$. Since the HLL solver fails to capture contact discontinuities, which are certainly produced in a complex flow, this test shows the importance of using an advanced Riemann solver like the Osher-type that we have adopted.

4.6. RHD Richtmyer–Meshkov instability

As a last test in two space dimensions, we have considered a simple case of the Richtmyer–Meshkov instability, which arises when a shock wave crosses a contact discontinuity within a fluid (Richtmyer, 1960; Meshkov, 1968). The numerical domain is $\Omega = [0, 100] \times [0, 5]$, and it is initially covered by a level zero grid with 600×30 cells. The fluid is initially at rest ($v_x = 0, v_y = 0$), with a jump in the density between two states separated by a sinusoidal perturbation at $x_0 + a \sin(\pi/2 + 2\pi y/\lambda)$, where $x_0 = 3, a = 0.25$ and $\lambda = 2.5$. At time $t = 0$ a single shock wave is placed at $x = 1$ and propagates towards the right with a prescribed Lorentz factor W_s . The shock wave is built after solving the relativistic Rankine–Hugoniot conditions (Taub, 1948). The purpose of this test is not to perform a detailed physical analysis of the Richtmyer–Meshkov instability in the relativistic regime, but rather to show the ability of the numerical scheme in handling large Lorentz factor flows. After the initial shock wave hits the sinusoidal interface, the standard development of the instability, well documented in Newtonian experiments and

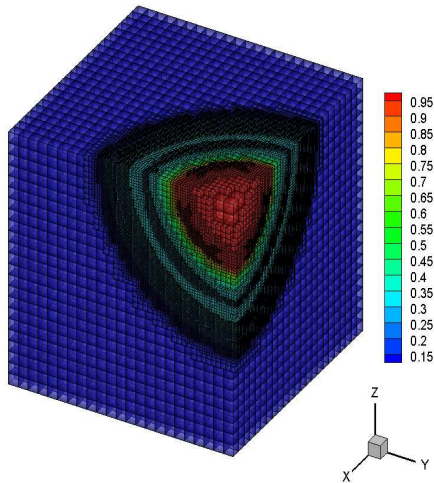


Figure 12: AMR grid structure at time $t = 0.25$ in the spherical explosion problem. The color contour of the rest-mass density is also shown.

simulations [see Brouillette (2002) for a review], generates a series of ”mushroom” structures, which have the net effect of mixing the fluid at either sides of the initial discontinuity.

This is also the case in the relativistic regime, but only for moderate Lorentz factors. Indeed, as reported in Fig. 10, the typical phenomenology of the Richtmyer–Meshkov instability is produced in a model with $W_s = 1.1$. On the contrary, Fig. 11 corresponds to a model with $W_s = 10$ and relativistic Mach number $\mathcal{M}_s = 32.2$, for which the Richtmyer–Meshkov instability is essentially suppressed (see also Mohseni et al. (2013)). We emphasize that, in this test with high Lorentz factor, the conversion from the conserved to the primitive variables is better obtained when the second strategy described in Section 2 is adopted, namely when Eq. (17) is solved.

4.7. RHD three-dimensional spherical explosion

In order to validate the numerical scheme also in three spatial dimensions, we solve the special relativistic explosion problem on the computational domain $\Omega = [-1; 1]^3$, with initial conditions given by

$$(\rho, v, p) = \begin{cases} (1.0, 0, 1) & \text{for } r \leq R, \\ (0.125, 0, 0.1) & \text{for } r > R, \end{cases} \quad (57)$$

where the radial coordinate $r = \sqrt{x^2 + y^2 + z^2}$, while $R = 0.4$ denotes the radius of the initial discontinuity. In practice, the initial flow variables take the same constant values of the classical Sod’s problem (Sod, 1978). The adiabatic index of the ideal-gas equation of state has been set to $\gamma = 4/3$. Due to the symmetry of the problem, the solution can be compared with an equivalent one dimensional problem in the radial direction r , which we have solved using the ECHO code by Del Zanna et al. (2007) with a high resolution uniform grid composed of 3000 cells. The initial grid at level zero of this three-dimensional problem uses $48 \times 48 \times 48$ cells, while during

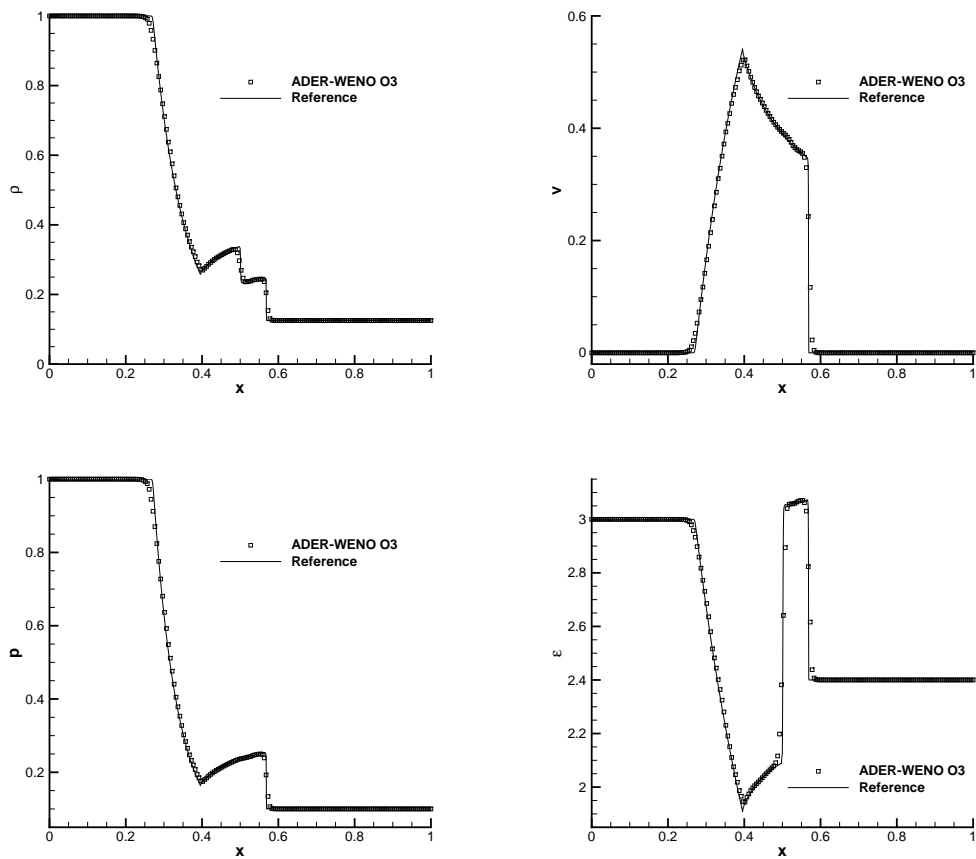


Figure 13: Explosion test in three space dimensions. From top left to bottom right: comparison of the 1D reference solution with the numerical solution obtained with a third order ADER-WENO scheme on an AMR mesh at time $t = 0.25$. One-dimensional cuts along the x -axis are shown for density, velocity, pressure and specific internal energy. Note that the plotted numerical data are the result of an interpolation, and are uniformly distributed.

the evolution we have chosen $\tau = 2$ and $\ell_{\max} = 3$. We have performed a calculation at third order accuracy with the Osher-type Riemann solver and reconstruction in characteristic variables. The AMR grid at the final time $t = 0.25$ is shown in Fig. 12 and is formed by 7,044,376 elements. We stress that the a totally refined uniform grid corresponding to this configuration would be composed by 56,623,104 elements. One dimensional profiles of the most relevant quantities along the x axis are reported in the four panels of Fig. 13. A very good agreement with the one-dimensional reference solution is obtained.

4.8. RMHD circularly-polarized Alfvén Wave: convergence test

Alfvén waves in ideal relativistic MHD have been studied in detail by Komissarov (1997), while the solution for a large amplitude circularly-polarized Alfvén wave was described by Del Zanna et al. (2007). Being analytic, the latter solution is particularly convenient to perform an analysis of the convergence properties of our numerical scheme. In practice, the magnetic field is given by

$$B_x = B_0 \quad (58)$$

$$B_y = \eta B_0 \cos[k(x - v_A t)] \quad (59)$$

$$B_z = \eta B_0 \sin[k(x - v_A t)], \quad (60)$$

where B_0 is the uniform magnetic field in the direction of propagation of the wave (the x direction), η is the amplitude of the wave, which can be arbitrarily large, k is the wave number, while v_A is the Alfvén speed, which can be shown to be (Del Zanna et al., 2007)

$$v_A^2 = \frac{B_0^2}{\rho h + B_0^2(1 + \eta^2)} \left[\frac{1}{2} \left(1 + \sqrt{1 - \left(\frac{2\eta B_0^2}{\rho h + B_0^2(1 + \eta^2)} \right)^2} \right) \right]^{-1}. \quad (61)$$

The transverse velocity field, with vector tips describing circles in the plane normal to \vec{B}_0 (the yz plane), is

$$v_y = -v_A B_y / B_0, \quad v_z = -v_A B_z / B_0. \quad (62)$$

Since the wave is incompressible, the background values of ρ and p are not affected, and the wave propagates with speed given by v_A . In our calculation we have used $\rho = p = B_0 = \eta = 1$. We have performed this test in two spatial dimensions, using periodic boundary conditions, over the computational domain $\Omega = [0; 2\pi] \times [0; 2\pi]$. After one period $T = L/v_A = 2\pi/v_A$, we compare the numerical solution with the analytic one at time $t = 0$. Fig. 14 shows the result of a representative calculation at the fourth order of accuracy, and the comparison with the exact solution. In order to verify the effective convergence rates of the numerical scheme, we have reported in Table 3 an analysis of the L_2 norms of the error of v_y (computed with respect to the reference solution as explained above) and the corresponding orders of convergence. This analysis has been performed with the HLL flux, $\ell_{\max} = 2$, CFL = 0.8 and using the minimum refinement factor allowed by the numerical scheme, which, we recall, is $\tau = 2$ for $M = 2$ and $\tau = 3$ for $M = 3$. Tab. 3 shows that the nominal order of convergence is essentially confirmed. The fourth order version of the scheme performs comparatively better than the third order one.

In addition, we have also compared a simple AMR simulation, that uses $\ell_{\max} = 1$, $\tau = 2$ starting from an initial grid with 20×20 cells, with two simulations performed over uniform grids, the first one corresponding to the coarse grid of the AMR case, and the second one corresponding to

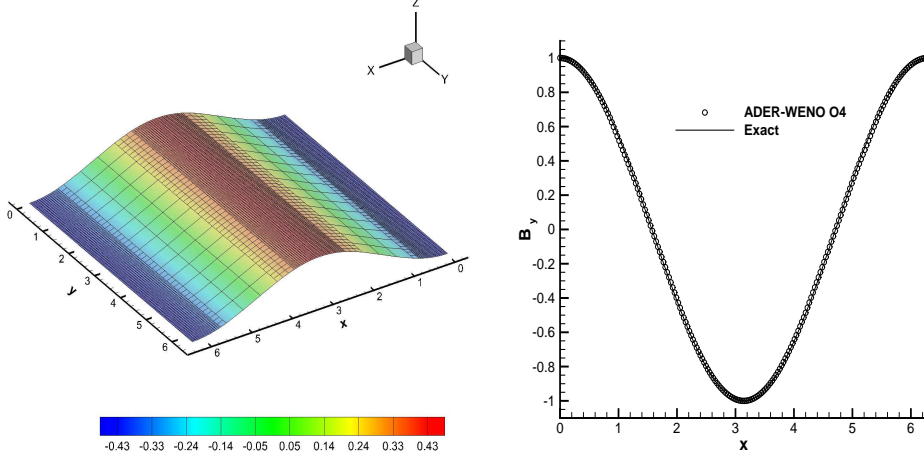


Figure 14: Solution of the circularly-polarized Alfvén Wave problem with the fourth order ADER-WENO scheme at time $t = T$. Left panel: distribution of v_y over the AMR grid. Right panel: comparison of the numerical and of the exact solution for B_y .

Table 3: Numerical convergence results for the circularly-polarized Alfvén wave test using the third and the fourth order version of the one-step ADER-WENO finite volume scheme. The error norms refer to the v_y component of the velocity at the final time $t = T$.

$\ell_{\max} = 2$					
N_G	ϵ_{L_2}	$\mathcal{O}(L_2)$	N_G	ϵ_{L_2}	$\mathcal{O}(L_2)$
$\mathcal{O}3$			$\mathcal{O}4$		
25	4.1159E-02		15	6.7463E-03	
30	2.6681E-02	2.37	20	2.1505E-03	3.97
35	1.8184E-02	2.48	25	7.6842E-04	4.61
40	1.3008E-02	2.51	30	3.1766E-04	4.84
45	9.7234E-03	2.47	35	1.5723E-04	4.56
50	7.5300E-03	2.42	40	8.5133E-05	4.59

the fine grid of the AMR case. The results of this comparison are reported in Tab. 4. As expected, the error of the AMR simulation, denoted as (b) in the Table, falls between those performed over the two uniform grids, denoted as (a) and (c), respectively. The last column of the table shows the CPU time, normalized to the simulation on the coarse uniform mesh, and it gives evidence that the effort inherent to the AMR implementation is largely justified.

4.9. RMHD relativistic shock tube problem

The new scheme has been validated also through one-dimensional shock tube problems. For brevity, we report here only the fifth test among those presented by Balsara (2001), with initial conditions given by

$$(\rho, v_x, v_y, v_z, p, B_y, B_z) = \begin{cases} (1.08, 0.4, 0.3, 0.2, 0.95, 0.3, 0.3) & \text{if } x \in [0; 0.5] \\ (1.0, -0.45, -0.2, 0.2, 1.0, -0.7, 0.5) & \text{if } x \in [0.5; 1]. \end{cases} \quad (63)$$

Table 4: Comparison of the error and of the CPU time using (a) a uniform coarse grid with 20×20 elements, (b) an AMR grid with $\ell_{\max} = 1$, $\tau = 2$ and (c) a uniform fine grid with 40×40 elements. The test adopts the circularly-polarized Alfven wave using a third order ADER-WENO scheme. The CPU time is normalized with respect to the simulation on the coarse uniform mesh.

	Cells at $t = T$	$\epsilon_{L_2}(v_y)$	CPU time
(a) Uniform Coarse	400	8.7703E-02	1.0
(b) AMR	1000	3.8007E-02	4.98
(c) Uniform Fine	1600	1.3273E-02	7.91

The magnetic field along the x direction is continuous across the discontinuity, and it is given by $B_x = 2.0$. The adiabatic index of the ideal gas is $\gamma = 1.6666$, and the problem is evolved to the final time $t_f = 0.55$. Seven waves are produced as the Riemann fan opens: a fast shock, an Alfven wave and a slow rarefaction, which propagate to the left; the usual contact discontinuity; and a slow shock, an Alfven wave and a fast shock, which propagate to the right. We have performed this test at the fourth order of accuracy with the HLL Riemann solver, using $\ell_{\max} = 2$, $\tau = 3$, starting from an initial uniform grid with 180 cells. The results of the calculations are reported in Fig. 15, where they are compared with the exact solution obtained with the Riemann solver of Giacomazzo and Rezzolla (2006).

4.10. RMHD Rotor Problem

In the MHD rotor problem proposed by Balsara and Spicer (1999) strong torsional Alfven waves propagate from a spinning cylinder embedded in a light fluid. The relativistic version of this test has been solved by Del Zanna et al. (2003) while resistivity effects were considered by Dumbser and Zanotti (2009). The rotor has a radius $R_0 = 0.1$, it is placed at the center of the computational domain $\Omega = [-0.6; 0.6] \times [-0.6; 0.6]$ and it is rotating with an angular frequency $\omega_s = 8.5$. The density is $\rho = 10$ inside the rotor and $\rho = 1$ in the ambient fluid at rest, while the adiabatic index of the gas is $\gamma = 4/3$. The pressure $p = 1$ is uniform everywhere, as well as the magnetic field, which, initially, has only one non-vanishing component, namely $B_x = 1$. The fact that B_x is initially constant everywhere allows the transport of angular momentum from the rotor to the ambient through the torsional Alfven waves. We have not applied any taper in the density of the rotor. Finally, transmissive boundary conditions are applied at the outer boundaries. We have solved this problem with the fourth order ADER-WENO scheme, starting with an initially uniform grid with 70×70 elements. During the evolution, AMR is activated with relevant parameters given by $\tau = 3$ and $\ell_{\max} = 2$. Fig. 16 shows the AMR mesh (left panels) and the pressure field (right panels) at the three different times $t = 0.1$, $t = 0.2$ and $t = 0.3$ (from top to bottom). Also in this test, but only in a limited number of troubled cells at the border between the rotor and the ambient medium, the accuracy of the solution has been intentionally reduced to first-order according to the MOOD-type approach of Clain et al. (2011).

4.11. RMHD Orszag–Tang

As a final test for magnetized flows we have considered the relativistic version of the Orszag–Tang vortex problem, which was first introduced by Orszag and Tang (1979) and later studied by

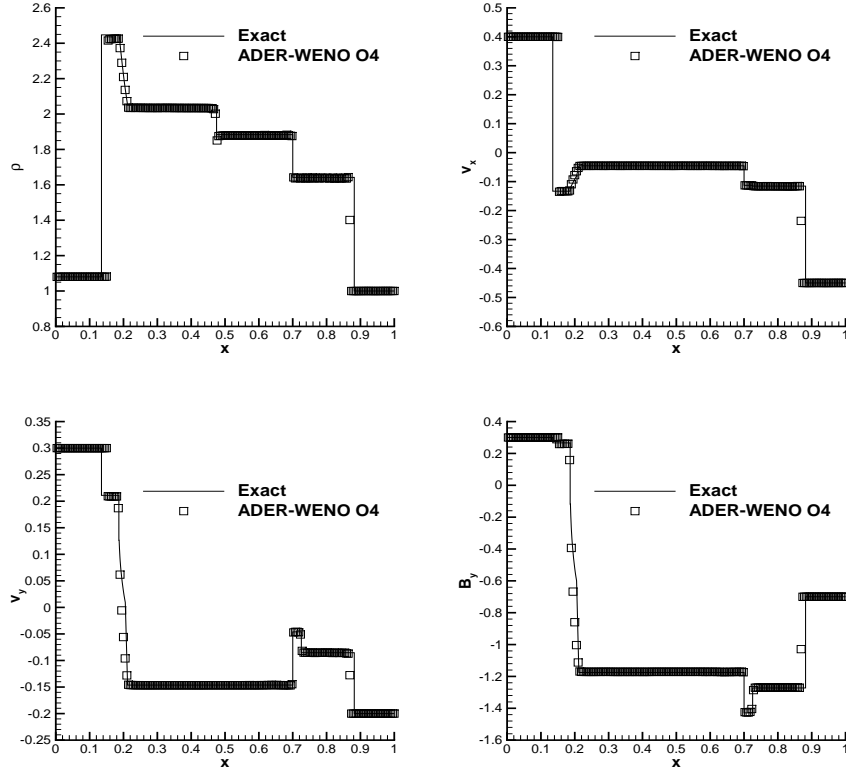


Figure 15: Solution of the RMHD shock tube with the fourth order ADER-WENO scheme at time $t = 0.55$. Dahlburg and Picone (1989) and Jiang and Wu (1999). The initial conditions are given by

$$\left(\rho, v_x, v_y, v_z, p, B_x, B_y, B_z\right) = \left(1, -\frac{v_0}{\sqrt{2}} \sin(y), \frac{v_0}{\sqrt{2}} \sin(x), 0, 1, -B_0 \sin(y), B_0 \sin(2x), 0\right), \quad (64)$$

where $v_0 = 0.75$, and $\gamma = 4/3$. The problem is solved up to $t = 4.0$ over the computational domain $\Omega = [0; 2\pi] \times [0; 2\pi]$. The initial grid at level zero uses 100×100 cells, while during the evolution we have chosen $\tau = 3$ and $\ell_{\max} = 2$. The calculation has been performed at the third order of accuracy with the HLL Riemann solver. The results are shown in the six panels of Fig. 17 at times $t = 0.5$, $t = 2.0$ and $t = 4.0$, where the AMR grids (left column) and the thermal pressure (right column) can be seen. They are in good agreement with the high conductivity limit of the same test by Dumbser and Zanotti (2009).

5. Conclusions

Extending our recent work about classical gas dynamics (Dumbser et al., 2013), we have presented the first implementation of ADER methods in combination with Adaptive Mesh Refinement for the solution of the special relativistic magnetohydrodynamics equations. The key idea of the ADER strategy, in the modern version proposed by Dumbser et al. (2008b), is to build high order accurate one-step finite volume schemes which are based on a high order nonlinear WENO reconstruction operator and an element-local weak formulation of the governing partial differential equations in space-time. Under many respects, by treating space and time on an equal

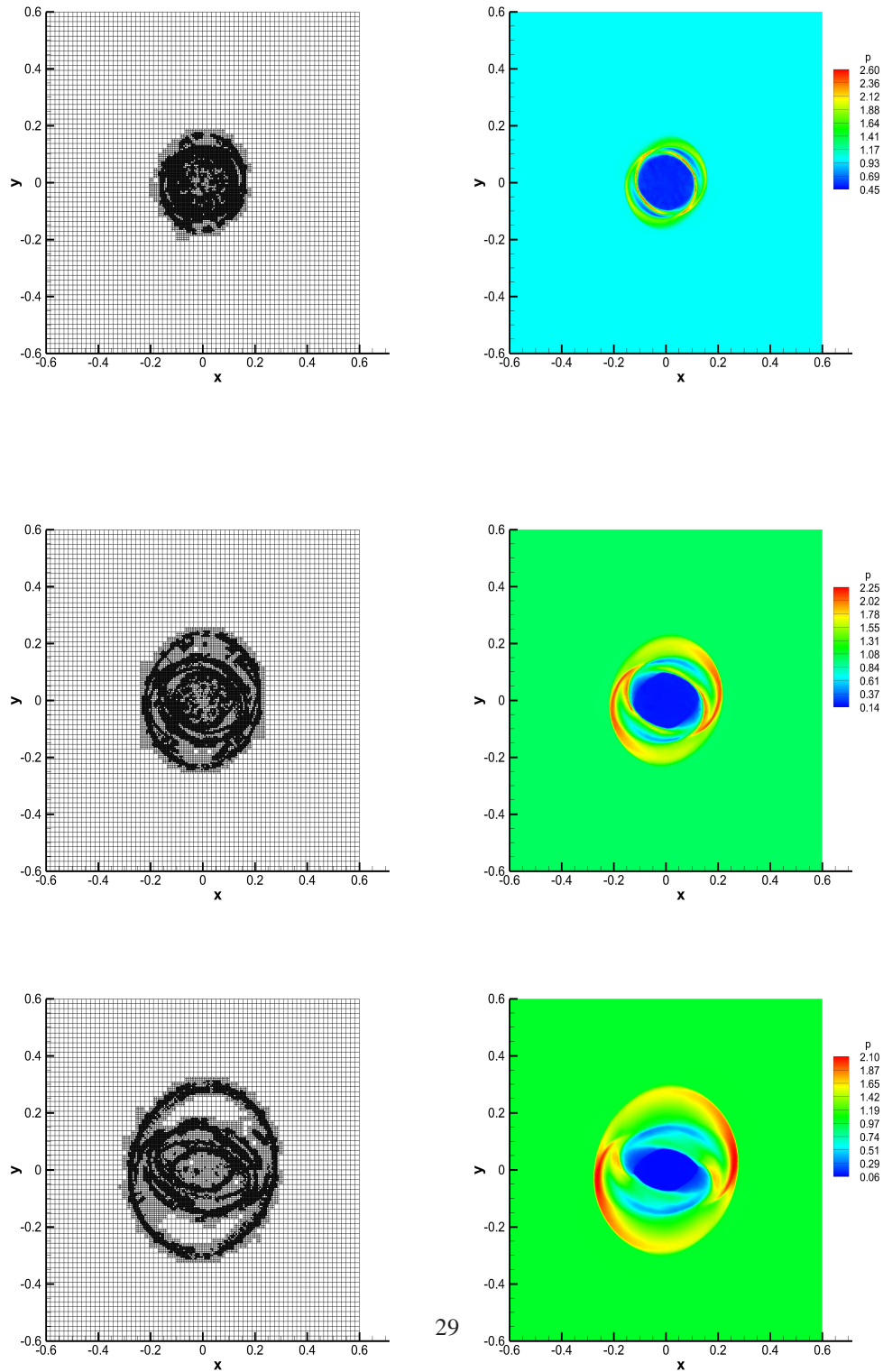


Figure 16: Two-dimensional relativistic Rotor problem at time $t = 0.1$, $t = 0.2$ and $t = 0.3$ (from top to bottom). The left columns show the AMR grid while the right columns show the pressure field. A fourth order ADER-WENO scheme with the HLL Riemann solver has been adopted. The initial grid has 60×60 cells, subsequently refined with $\ell_{\max} = 2$ and $\tau = 3$.

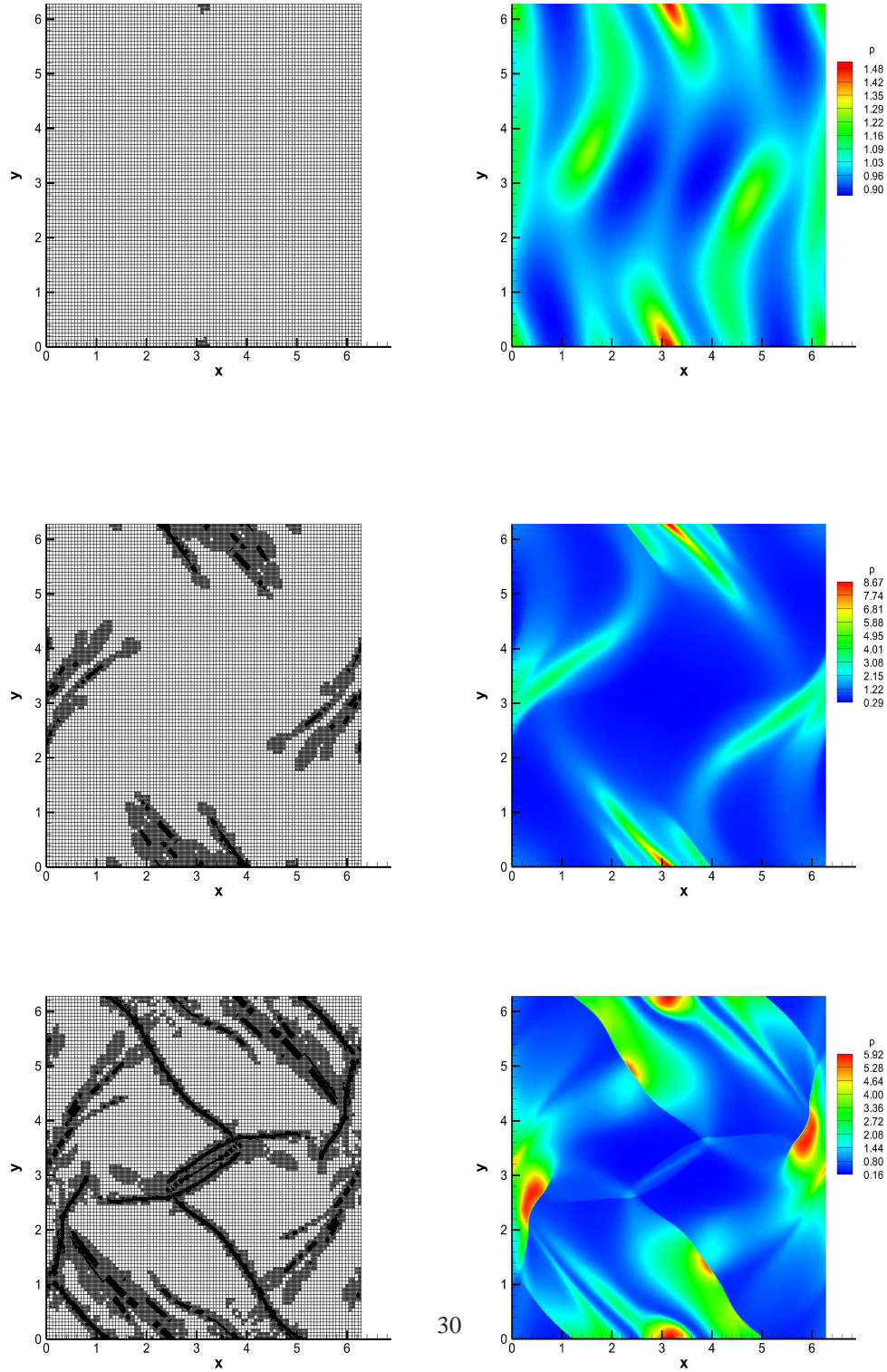


Figure 17: Two-dimensional relativistic Orszag–Tang vortex problem at time $t = 0.5$, $t = 2.0$ and $t = 4.0$ (from top to bottom). The left columns show the AMR grid while the right columns show the pressure field. A third order ADER-WENO scheme with the HLL Riemann solver has been adopted. The initial grid has 100×100 cells, subsequently refined with $\ell_{\max} = 2$ and $\tau = 3$.

footing, the ADER scheme calls naturally for an implementation to the relativistic regime. Its property becomes also particularly advantageous in the presence of AMR, since, by avoiding the sub-steps typical of Runge–Kutta schemes, it substantially reduces the amount of necessary MPI communications and makes the implementation of time-accurate local time stepping (LTS) very natural and simple. Our AMR implementation follows a ‘cell-by-cell’ refinement criterion through a tree-data structure, similarly to Khokhlov et al. (1997).

We have verified the ability of our new scheme in coping with complex physical conditions, by considering a wide set of relativistic hydrodynamic and magnetohydrodynamic tests, both for one and for multi-dimensional problems. Our ADER-WENO AMR scheme represents the first step of a plan to incorporate more physical effects (viscous fluids, radiation hydrodynamics etc.) into a versatile tool suitable for studying high energy relativistic processes in astrophysics with high order of accuracy in both space and time.

High order methods often become the only choice for problems characterized by a wide range of length-scales, and in particular when fluid instabilities are triggered. One of such cases is represented by the Richtmyer–Meshkov (RM) instability, which arises when a shock wave crosses the interface between two fluids having different densities. The RM instability is thought to play a significant role in several high energy physical systems, including inertial confinement fusion (ICF) and core-collapse supernovae explosions. Broadly speaking, it typically produces a pronounced mixing of the involved fluids. Relativistic effects on the RM instability have been considered only recently (Inoue, 2012; Matsumoto and Masada, 2013; Mohseni et al., 2013), showing, somewhat counter-intuitively, that the growth rate of the instability decreases as the Lorentz factor increases. In the near future we plan to shed light on these aspects by means of high order numerical simulations combined with space-time adaptive mesh refinement.

Acknowledgments

We would like to thank Davide Radice and Francesco Fambri for useful discussions; Bruno Giacomazzo for providing the exact Riemann solver for the RMHD equations, as well as an anonymous referee for various suggestions that allowed us to improve the quality of this work. The research conducted here has been financed in parts by the European Research Council under the European Union’s Seventh Framework Programme (FP7/2007-2013) in the frame of the research project *STiMulUs*, ERC Grant agreement no. 278267.

The numerical simulations presented in this paper were performed on the FERMI super-computer at CINECA (Italy) within the IsB05-STiMulUs project and on SuperMuc at Leibniz-Rechenzentrum (Germany), within the PRACE 6-th CALL (Project ID 2012071312).

References

- M.A. Aloy, J.M. Ibáñez, J.M. Martí, E. Müller, *Astrophys. J. Suppl.* 122 (1999) 151–166.
- M.A. Aloy, L. Rezzolla, *Astrophys. J.* 640 (2006) L115–L118.
- M. Anderson, E. Hirschmann, S.L. Liebling, D. Neilsen, *Classical Quantum Gravity* 23 (2006) 6503–6524.
- A.M. Anile, *Relativistic Fluids and Magneto-fluids*, Cambridge University Press, 1990.
- A.M. Anile, J.C. Miller, S. Motta, *Physics of Fluids* 26 (1983) 1450–1460.
- L. Antón, J.A. Miralles, J.M. Martí, J.M. Ibáñez, M.A. Aloy, P. Mimica, *Astrophys. J. Suppl.* 188 (2010) 1–31.
- A. Baeza, A. Martínez-Gavara, P. Mulet, *Applied Numerical Mathematics* 62 (2012) 278–296.
- A. Baeza, P. Mulet, *International Journal for Numerical Methods in Fluids* 52 (2006) 455–471.
- L. Baiotti, *Numerical relativity simulations of non-vacuum spacetimes in three dimensions*, Ph.D. thesis, SISSA, International School for advanced studies, 2004.
- D. Balsara, *Astrophysical Journal Suppl. Series* 132 (2001) 83–101.

- D.S. Balsara, D.S. Spicer, *J. Comput. Phys.* 149 (1999) 270–292.
- K. Beckwith, J.M. Stone, *The Astrophysical Journal Supplement Series* 193 (2011) 6.
- M.J. Berger, *SIAM Journal of Scientific and Statistical Computing* 7 (1986) 904–916.
- M.J. Berger, P. Colella, *J. Comput. Phys.* 82 (1989) 64–84.
- M.J. Berger, J. Olinger, *J. Comput. Phys.* 53 (1984) 484–512.
- M. Brouillette, *Annual Review of Fluid Mechanics* 34 (2002) 445–468.
- N. Bucciantini, L. Del Zanna, *Astron. Astrophys.* 528 (2011) A101.
- M.W. Choptuik, in: C. Evans, L. Finn, D. Hobill (Eds.), *Frontiers in Numerical Relativity*, Cambridge University Press, Cambridge, England, 1989, pp. 206–221.
- S. Clain, S. Diot, R. Loubère, *Journal of Computational Physics* 230 (2011) 4028–4050.
- R.B. Dahlburg, J.M. Picone, *Phys. Fluids B* 1 (1989) 2153–2171.
- F. De Colle, J. Granot, D. López-Cámara, E. Ramirez-Ruiz, *Astrophys. J.* 746 (2012) 122.
- A. Dedner, F. Kemm, D. Kröner, C.D. Munz, T. Schnitzer, M. Wesenberg, *Journal of Computational Physics* 175 (2002) 645–673.
- L. Del Zanna, N. Bucciantini, *Astron. Astrophys.* 390 (2002) 1177–1186.
- L. Del Zanna, N. Bucciantini, P. Londrillo, *Astron. Astrophys.* 400 (2003) 397–413.
- L. Del Zanna, O. Zanotti, N. Bucciantini, P. Londrillo, *Astron. Astrophys.* 473 (2007) 11–30.
- K. Dionysopoulou, D. Alic, C. Palenzuela, L. Rezzolla, B. Giacomazzo, *Phys. Rev. D* 88 (2013) 044020.
- A. Dolezal, *Journal of Computational Physics* 120 (1995) 266–277.
- O. Dönmez, *Astrophys. Spac. Sci.* 293 (2004) 323–354.
- M. Dumbser, D.S. Balsara, E.F. Toro, C.D. Munz, *Journal of Computational Physics* 227 (2008a) 8209–8253.
- M. Dumbser, C. Enaux, E.F. Toro, *Journal of Computational Physics* 227 (2008b) 3971–4001.
- M. Dumbser, M. Kaeser, V.A. Titarev, E.F. Toro, *Journal of Computational Physics* 226 (2007) 204–243.
- M. Dumbser, M. Kser, E.F. Toro, *Geophysical Journal International* 171 (2007) 695–717.
- M. Dumbser, E. Toro, *Communications in Computational Physics* 10 (2011) 635–671.
- M. Dumbser, O. Zanotti, *Journal of Computational Physics* 228 (2009) 6991–7006.
- M. Dumbser, O. Zanotti, A. Hidalgo, D.S. Balsara, *Journal of Computational Physics* 248 (2013) 257–286.
- W.E. East, F. Pretorius, B.C. Stephens, *Phys. Rev. D* 85 (2012) 124010.
- Z.B. Etienne, Y.T. Liu, S.L. Shapiro, *Phys. Rev. D* 82 (2010) 084031.
- E. Evans, S. Iyer, E. Schnetter, W.M. Suen, J. Tao, R. Wolfmeyer, H.M. Zhang, *Phys. Rev. D* 71 (2005) 081301(R).
- J.A. Font, *Living Rev. Relativ.* 6 (2008) 4; <http://www.livingreviews.org/lrr-2008-7>.
- G. Gassner, F. Lörcher, C.D. Munz, *Journal of Scientific Computing* 34 (2008) 260–286.
- B. Giacomazzo, L. Rezzolla, *Journal of Fluid Mechanics* 562 (2006) 223–259.
- A. Harten, B. Engquist, S. Osher, S.R. Chakravarthy, *Journal of Computational Physics* 71 (1987) 231–303.
- A. Harten, P.D. Lax, B. van Leer, *SIAM Rev.* 25 (1983) 35.
- T. Inoue, *Astrop. J.* 760 (2012) 43.
- G. Jiang, C. Wu, *Journal of Computational Physics* 150 (1999) 561–594.
- G.S. Jiang, C.W. Shu, *J. Comput. Phys.* 126 (1996) 202–228.
- A.M. Khokhlov, E.S. Oran, J.C. Wheeler, *Astrophys. J.* 478 (1997) 678.
- S.S. Komissarov, *Physics Letters A* 232 (1997) 435–442.
- S.S. Komissarov, *Mon. Not. R. Astron. Soc.* 303 (1999) 343–366.
- L. Lehner, C. Palenzuela, S.L. Liebling, C. Thompson, C. Hanna, *Phys. Rev. D* 86 (2012) 104035.
- S.L. Liebling, L. Lehner, D. Neilsen, C. Palenzuela, *Phys. Rev. D* 81 (2010) 124023.
- X.D. Liu, S. Osher, T. Chan, *Journal of Computational Physics* 115 (1994) 200–212.
- R. Löhner, *Computer Methods in Applied Mechanics and Engineering* 61 (1987) 323–338.
- F. Lörcher, G. Gassner, C.D. Munz, *Journal of Scientific Computing* 32 (2007) 175–199.
- A. Lucas-Serrano, J.A. Font, J.M. Ibanez, J.M. Martí, *Astron. Astrophys.* 428 (2004) 703–715.
- P. MacNeice, K.M. Olson, C. Mobarry, R. de Fainchtein, C. Packer, *Computer Physics Communications* 126 (2000) 330–354.
- J.M. Martí, J.M. Ibáñez, J.A. Miralles, *Phys. Rev. D* 43 (1991) 3794.
- J.M. Martí, E. Müller, *J. Fluid Mech.* 258 (1994) 317–333.
- J.M. Martí, E. Müller, *Living Rev. Relativ.* 6 (2003) 7; <http://www.livingreviews.org/lrr-2003-7>.
- J. Matsumoto, Y. Masada, *Astrop. J. Lett.* 772 (2013) L1.
- E. Meshkov, *Fluid Dynamics* 43 (1968) 101–104.
- A. Mignone, G. Bodo, *Mon. Not. R. Astron. Soc.* 364 (2005) 126–136.
- A. Mignone, M. Ugliano, G. Bodo, *Monthly Notices of the Royal Astronomical Society* 393 (2009) 1141–1156.
- A. Mignone, C. Zanni, P. Tzeferacos, B. van Straalen, P. Colella, G. Bodo, *Astrophys. J. Suppl. Ser.* 198 (2012) 7.
- F. Mohseni, M. Mendoza, S. Succi, H.J. Herrmann, *ArXiv e-prints* (2013).
- S.A. Orszag, C.M. Tang, *Journal of Fluid Mechanics* 90 (1979) 129.

- C. Palenzuela, L. Lehner, O. Reula, L. Rezzolla, *Mon. Not. R. Astron. Soc.* 394 (2009) 1727–1740.
- D. Radice, L. Rezzolla, *Phys. Rev. D* 84 (2011) 024010.
- D. Radice, L. Rezzolla, *Astron. Astrophys.* 547 (2012) A26.
- L. Rezzolla, O. Zanotti, *Journ. of Fluid Mech.* 449 (2001) 395.
- L. Rezzolla, O. Zanotti, *Phys. Rev. Lett.* 89 (2002) 114501.
- L. Rezzolla, O. Zanotti, *Relativistic Hydrodynamics*, Oxford University Press, Oxford UK, 2013.
- L. Rezzolla, O. Zanotti, J.A. Pons, *Journ. of Fluid Mech.* 479 (2003) 199.
- R.D. Richtmyer, *Communications on Pure and Applied Mathematics* 13 (1960) 297–319.
- G.A. Sod, *Journal of Computational Physics* 27 (1978) 1–31.
- P. Solin, *Partial Differential Equations And the Finite Element Method*, Pure and Applied Mathematics, Wiley-Interscience, 2006.
- J. Tao, W.M. Suen, R. Wolfmeyer, H.M. Zhang, in: *APS April Meeting Abstracts*, p. K1012.
- A.H. Taub, *Phys. Rev.* 74 (1948) 328–334.
- A. Taube, M. Dumbser, C.D. Munz, R. Schneider, *International Journal of Numerical Modelling: Electronic Networks, Devices and Fields* 22 (2009) 77–103. Cited By (since 1996):9.
- A. Tchekhovskoy, J.C. McKinney, R. Narayan, *Mon. Not. R. Astron. Soc.* 379 (2007) 469–497.
- E.F. Toro, *Riemann Solvers and Numerical Methods for Fluid Dynamics*, Springer-Verlag, 2009.
- E.F. Toro, V.A. Titarev, *Proceedings of the Royal Society of London. Series A: Mathematical, Physical and Engineering Sciences* 458 (2002) 271–281.
- E.F. Toro, V.A. Titarev, *Journal of Computational Physics* 202 (2005) 196–215.
- B. van der Holst, R. Keppens, Z. Meliani, *Computer Physics Communications* 179 (2008) 617–627.
- K.H.A. Winkler, M.L. Norman, D. Mihalas, *Journal of Quantitative Spectroscopy and Radiative Transfer* 31 (1984) 473–478.
- O. Zanotti, M. Dumbser, *Mon. Not. R. Astron. Soc.* 418 (2011) 1004–1011.
- W. Zhang, A. MacFadyen, *The Astrophysical Journal Supplement Series* 164 (2006) 255.

Appendix A.

We list the most relevant parameters of the polynomials used in the WENO reconstruction that we have described in Sect. 3.2. Table A.5 reports the coordinates λ_k of the Gauss-Legendre quadrature nodes and the corresponding nodal basis of polynomials ψ_l , for a few values of M up to $M = 4$. On the other hand, Fig. (A.18) shows the corresponding one-dimensional stencils that are used.

Table A.5: The table shows the coordinates of the Gauss–Legendre nodes and the corresponding nodal basis polynomials for a few values of M .

λ_k	ψ_l
$M = 1$	
$\lambda_1 = 0.2113248654051$	$\psi_1 = 1.366025403784 - 1.732050807568\xi$
$\lambda_2 = 0.7886751345948$	$\psi_2 = -0.3660254037844 + 1.732050807568\xi$
$M = 2$	
$\lambda_1 = 0.1127016653792$	$\psi_1 = 1.478830557701 - 4.624327782069\xi + 3.333333333333\xi^2$
$\lambda_2 = 0.5$	$\psi_2 = -0.66666666666666 + 6.6666666666666\xi - 6.6666666666666\xi^2$
$\lambda_3 = 0.8872983346207$	$\psi_3 = 0.1878361089654 - 2.042338884597\xi + 3.333333333333\xi^2$
$M = 3$	
$\lambda_1 = 6.9431844202973 \times 10^{-2}$	$\psi_1 = 1.526788125457 - 8.546023607872\xi + 14.32585835417\xi^2 - 7.42054006803894\xi^3$
$\lambda_2 = 0.3300094782075$	$\psi_2 = -0.8136324494869 + 13.80716692568\xi - 31.38822236344\xi^2 + 18.79544940755\xi^3$
$\lambda_3 = 0.6699905217924$	$\psi_3 = 0.4007615203116 - 7.417070421462\xi + 24.99812585921\xi^2 - 18.79544940755\xi^3$
$\lambda_4 = 0.9305681557970$	$\psi_4 = -0.1139171962819 + 2.155927103645\xi - 7.935761849944\xi^2 + 7.420540068038\xi^3$
$M = 4$	
$\lambda_1 = 4.6910077030668 \times 10^{-2}$	$\psi_1 = 1.551408049094 - 13.47028450119\xi + 38.64449905534\xi^2 - 44.98898505587\xi^3 + 18.33972111443\xi^4$
$\lambda_2 = 0.2307653449471$	$\psi_2 = -0.8931583920000 + 22.92433355572\xi - 88.22281082816\xi^2 + 117.8634151266\xi^3 - 51.93972111443\xi^4$
$\lambda_3 = 0.5$	$\psi_3 = 0.5333333333333 - 14.93333333333\xi + 82.13333333333\xi^2 - 134.4000000000\xi^3 + 67.20000000000\xi^4$
$\lambda_4 = 0.7692346550528$	$\psi_4 = -0.2679416522233 + 7.689927178385\xi - 46.27089213480\xi^2 + 89.89546933107\xi^3 - 51.93972111443\xi^4$
$\lambda_5 = 0.9530899229693$	$\psi_5 = 7.635866179581 \times 10^{-2} - 2.210642899581\xi + 13.71587057429\xi^2 - 28.36989940184\xi^3 + 18.33972111443\xi^4$

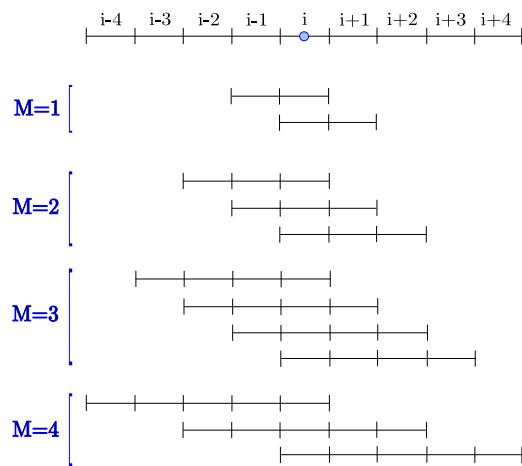


Figure A.18: Representation of the one-dimensional stencils adopted up to $M = 4$. Odd order schemes (even polynomials of degree M) always use three stencils, while even order schemes (odd polynomials of degree M) always adopt four stencils, with the exception of the $M = 1$ case, for which there are only two stencils.

